LETTER

doi:10.1038/nature10583

Grid cells without theta oscillations in the entorhinal cortex of bats

Michael M. Yartsev[1], Menno P. Witter[2] & Nachum Ulanovsky[1]

Grid cells provide a neural representation of space, by discharging when an animal traverses through the vertices of a periodic hexagonal grid spanning the environment[1]. Although grid cells have been characterized in detail in rats[1–6], the fundamental question of what neural dynamics give rise to the grid structure remains unresolved. Two competing classes of models were proposed: network models, based on attractor dynamics[7–9], and oscillatory interference models, which propose that interference between somatic and dendritic theta-band oscillations (4–10 Hz) in single neurons transforms a temporal oscillation into a spatially periodic grid[10–13]. So far, these models could not be dissociated experimentally, because rodent grid cells always co-exist with continuous theta oscillations[4–6,14]. Here we used a novel animal model, the Egyptian fruit bat[15,16], to refute the proposed causal link between grids and theta oscillations. On the basis of our previous finding from bat hippocampus, of spatially tuned place cells in the absence of continuous theta oscillations[17], we hypothesized that grid cells in bat medial entorhinal cortex might also exist without theta oscillations. Indeed, we found grid cells in bat medial entorhinal cortex that shared remarkable similarities to rodent grid cells. Notably, the grids existed in the absence of continuous theta-band oscillations, and with almost no theta modulation of grid-cell spiking—both of which are essential prerequisites of the oscillatory interference models. Our results provide a direct demonstration of grid cells in a non-rodent species. Furthermore, they strongly argue against a major class of computational models of grid cells.

To elucidate the cellular and network mechanisms of grid cells in mammalian entorhinal cortex, we conducted electrophysiological recordings in a megabat, *Rousettus aegyptiacus* (Egyptian fruit bat). This bat species[15] belongs to a different suborder of bats than the big brown bat[16], the hippocampus of which we studied previously[17,18]. Therefore, to set the foundations for subsequent entorhinal recordings in this bat species, we first examined neural activity in hippocampal area CA1 (Fig. 1a). Bats crawled in a large arena (Fig. 1b) in search of food, and the activity of individual neurons was recorded using tetrodes (Supplementary Figs 1 and 2). Of all the well-isolated excitatory neurons in CA1, 36% were classified as place cells, becoming active when the bat entered a particular region of the environment (23 out of 64 cells with spatial information >0.5 bits per spike). Locations of individual place fields spanned the entire experimental arena (Fig. 1c), similar to place cells in rats[19]. High-frequency ripple oscillations (120–160 Hz) were present in the local field potential (LFP) during sleep (Supplementary Fig. 3a), and were very similar in their properties to ripples in rat hippocampus[20] (Supplementary Fig. 3 and Supplementary Text). Hippocampal theta oscillations in the LFP occurred in short, intermittent bouts (Fig. 1d), lasting typically ~1 s, and these bouts in the behaving bat were separated with an average 19-s interval (Supplementary Fig. 4a–d)—markedly different from the continuous theta oscillations observed in locomoting rats[21], but similar to the intermittent theta bouts in monkeys[22] and humans[23]. Because of the sparse occurrence of these bouts, theta oscillations were not evident in spectral analysis of the LFP, neither during sleep (Fig. 1e, left), during behavioural sessions (right), nor as a function of the bat's velocity (Fig. 1f). Thus, in agreement with our previous findings in big brown bats[17], we found that in Egyptian fruit bats, hippocampal place cells existed in the absence of continuous theta oscillations in the LFP.

We next turned to studying the medial entorhinal cortex (MEC) of bats, the region where grid cells are most prevalent in rats[1–6]. As a first step, we determined the anatomical location and borders of MEC (Fig. 2a and Supplementary Figs 5 and 6). Immunohistochemical staining revealed that: (1) similar to rats[24], the dorsal border of bat MEC (postrhinal border) was clearly identifiable by an abrupt change in layer structure (Supplementary Fig. 6b, d) and an abrupt transition in parvalbumin and calretinin staining (Fig. 2a and Supplementary Figs 5 and 6); and (2) similar to rats, the bat MEC had a densely packed layer II, sparser layers III and V, and a layer IV (*lamina dissecans*) with very few cell bodies (Supplementary Figs 5 and 6). Thus, the overall structure of bat MEC was very similar to that of rat MEC.

We targeted our tetrode recordings to the dorsal-most part of MEC: the region where we expected to find grid cells with the tightest and most pronounced grid structure, as in rats[1,2]. The positions of all

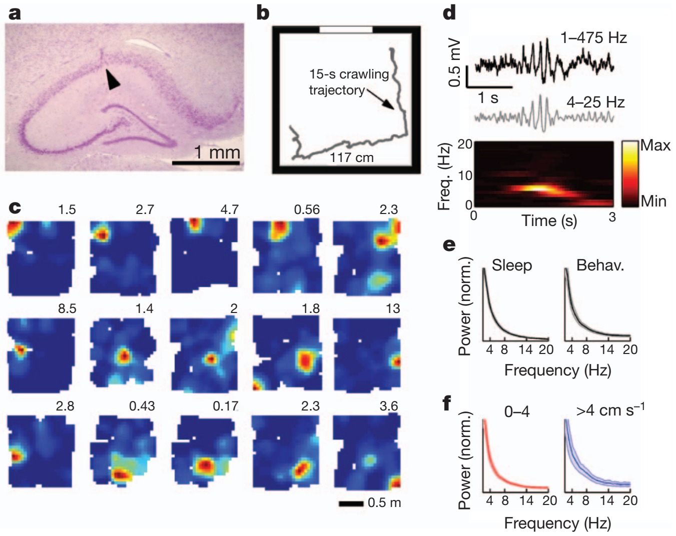

Figure 1 | Bat CA1 recordings demonstrate place cells but no continuous theta oscillations. **a**, Coronal section showing tetrode track in dorsal hippocampal area CA1 (arrowhead). **b**, Behavioural arena (117 × 117 cm) with white cue card. Grey line shows example 15-s crawling trajectory. **c**, Firing rate maps of 15 place cells, colour-coded from zero (blue) to maximum firing rate (red; value indicated). **d**, Example theta bout recorded during locomotion. Top: wideband LFP trace (1–475 Hz, black); middle, filtered trace (4–25 Hz, grey); bottom, spectrogram (frequency × time). **e**, LFP power spectrum during sleep (left) and behaviour (right) for all recording sites (mean ± s.e.m.). **f**, LFP power spectrum separated according to bat's velocity (indicated); normalized to power at 2 Hz. Note absence of peak at theta frequency.

---

[1]Department of Neurobiology, Weizmann Institute of Science, Rehovot 76100, Israel. [2]Kavli Institute for Systems Neuroscience and Centre for the Biology of Memory, Norwegian University of Science and Technology, NO-7489 Trondheim, Norway.

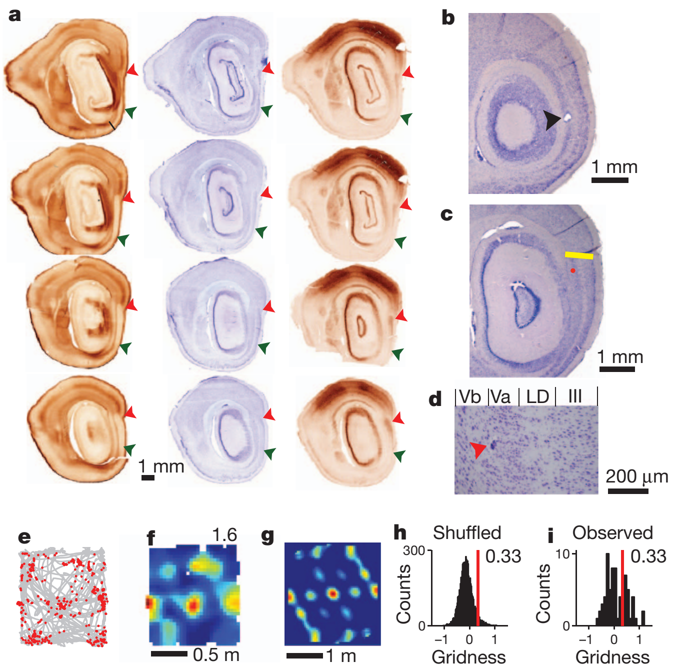

Figure 2 | Anatomical delineation of MEC in Egyptian fruit bats, and targeting of grid cells. **a**, Sagittal sections stained for calretinin (left), Nissl (middle) and parvalbumin (right), arranged from medial (top) to lateral (bottom). Arrowheads indicate MEC borders: dorsal, red; ventral, green. **b**, Electrolytic lesion at the end of a tetrode track (arrowhead). **c**, Recording location in MEC layer V (red dot), close to the dorsal (postrhinal) border of MEC (yellow line). **d**, Higher magnification of the recording location in **c** (arrowhead). MEC layers are indicated on top; LD, *lamina dissecans*[24] (layer IV). **e–g**, Grid cell recorded in the MEC location shown in **c**. **e**, Trajectory (grey line) and locations of spikes (red dots), showing the hexagonal firing pattern of a grid cell. **f**, Colour-coded rate map, with peak rate indicated. **g**, Spatial autocorrelogram of the rate map. **h**, Distribution of gridness for shuffled data (Supplementary Information), with 95th percentile indicated (red line; gridness = 0.33). **i**, Histogram of gridness values for all well-separated MEC neurons ($n = 70$). Neurons with gridness >0.33 were defined as grid cells ($n = 25$).

tetrodes were verified histologically by reconstructing the tetrode tracks and by electrolytic lesions (Fig. 2b–d and Supplementary Figs 7–9). Many MEC neurons were active at multiple locations in the arena (for example, Fig. 2e, f), and a hexagonal grid structure was revealed by computing the spatial autocorrelogram of their firing-rate map (Fig. 2g). To quantify the degree of 60° hexagonal rotational symmetry for each neuron, we employed a commonly used 'gridness' index[2] (Supplementary Fig. 10): a higher index indicates a more hexagonal firing field. To test statistically whether a neuron is a grid cell, we used a standard shuffling procedure[4–6] (Fig. 2h, i). Of the 70 well-isolated, behaviourally active neurons recorded in MEC, 36% were classified as grid cells (25 out of 70).

How similar are grid cells in bats versus rats? First, similar to rats[1], grid vertices were separated by 60° angles (Fig. 3a), as expected from a hexagonal structure, and individual firing fields were almost equally spaced (mean standard deviation of grid spacing across the six inner peaks: 6.8 cm; $n = 25$ grid cells). Second, as in rats[1–6], co-localized grid cells in superficial layers of MEC shared similar grid orientation (tilt) and spacing (Fig. 3b and Supplementary Information). Third, as in rats[1], cross-correlating the rate maps of simultaneously recorded grid cells revealed that their maps were offset in phase (Fig. 3c, central peaks of cross-correlograms are offset from the white cross), and the amount of offset spanned all possible phases (Fig. 3d). Fourth, as in rats[1], the grid spacing of individual cells increased with the cell's distance from the postrhinal border (Fig. 3e); this correlation was significant across all neurons ($r = 0.47$, $P < 0.025$), but was even more apparent when analysing separately each bat's data (bat 1, $r = 0.98$, $P < 0.02$; bat 2, $r = 0.67$, $P < 0.05$; bat 3, $r = 0.60$, $P = 0.07$). Fifth, as in rats[2], the firing rate increased with movement velocity (Fig. 3f; *t*-test, $t_{24} = 2.9$, $P < 0.001$). This correlation of firing rate and velocity probably explains the relatively low firing rates of MEC neurons in crawling bats (Fig. 3e, g) compared to rats[1–3,6], because bats crawled rather slowly (Supplementary Fig. 11). Finally, we found that in bat MEC, the diversity of spatial cell types was very similar to that known from rat MEC[1–6,25] and contained: (1) 'pure grid cells'[1,2] (Fig. 3g, lower-right quadrant; for example, cells 3, 4, 5), with no sensitivity to the animal's head direction[1,2]; (2) 'conjunctive grid cells'[2,6] (Fig. 3g, upper-right quadrant; cell 2), which are grid cells tuned to a specific head direction[2,6]; (3) head-direction cells[2] that have no grid structure (Fig. 3g, upper-left quadrant; cells 8, 9; see also Supplementary Fig. 12); and (4) 'border cells'[25], which fired along geometrical borders of the environment (for example, Fig. 3g, cell 6). Some cells that did not cross the shuffling thresholds still exhibited clear spatial patterns characteristic of grid cells (Fig. 3g, cell 10) or head-direction cells (cell 7). Taken together, these results indicate that the detailed properties of grid cells (and other cell types) in bat MEC were very similar to those in rat MEC.

We next turned to address the central question of this study, and asked whether the grids can exist without key elements of the oscillatory interference models[10–13]—namely, without continuous theta oscillations in the LFP, and in the absence of theta modulation of grid-cell firing. As a first step in studying the LFP in MEC, we examined non-theta-band, high-frequency ripple oscillations, which are most prominent during sleep[20] (Supplementary Fig. 3d). Ripples in bat MEC were very similar in their properties to ripples in rat MEC (Supplementary Fig. 3d–f and Supplementary Text). However, despite the similarity in ripple oscillations, bats differed markedly from rats in the nature of theta oscillations. First, unlike rats[4–6,14,26], we never observed a prominent continuous theta-band oscillation in the LFP, irrespective of the recording site in MEC and the type of reference used (Fig. 4a, b and Supplementary Information). The LFP power-spectrum showed no theta peak, neither during sleep (Supplementary Fig. 13, left), during behaviour (Fig. 4a,b, 'Behav.'), as a function of the animal's velocity (Fig. 4a, b, coloured panels), nor as a function of the bat's echolocation mode[17] (Supplementary Fig. 14a–d). Second, unlike the continuous theta oscillations typically observed in rat MEC[4,5,14,26], theta oscillations in bat MEC occurred in short intermittent bouts, both during behaviour (Fig. 4c–e and Supplementary Fig. 4f, h) and during sleep (Supplementary Fig. 4e, g), similar to bat CA1; 92% of theta bouts during behaviour had duration ≤1 s (Fig. 4d). Theta bouts were separated by very long inter-bout intervals (Fig. 4e; average interval: 37 ± 2 s; 18% of intervals were >1 min). The bat's velocity and echolocation rate were not different during theta bouts versus non-theta epochs (Supplementary Fig. 14e, f). Third, we computed the spike-train temporal autocorrelations for individual grid cells (Fig. 4f, top and Supplementary Fig. 15), and examined the degree of theta modulation in these autocorrelations by computing a standard 'theta index' that was used in previous studies in rats[4–6,26]; this index is based on the relative theta-band power in the Fourier transform of the temporal autocorrelation (Fig. 4g and Supplementary Information). Using either the same criterion that was employed previously to identify theta modulation in rat grid cells[6] (theta index >5), or using a statistical shuffling procedure for each individual spike train, we found that nearly all grid cells in bat MEC (24 out of 25) did not exhibit theta-modulated firing (Fig. 4h, left; theta index across all grid cells 1.29 ± 0.82 (mean ± s.d., maximal value 2.9)), irrespective of the bat's velocity (Supplementary Fig. 16). Because, in the rat MEC, neurons recorded in layers II and III show the most pronounced theta modulation of neuronal firing[6,27], we also analysed separately the data recorded from layers II and III of bat MEC; these analyses showed that no significant theta modulation was present in any of the 35 neurons (of all classes) recorded in layers II and III and in any of the multi-units from these layers (Supplementary Fig. 17). Fourth, because the firing of most neurons in rat MEC (especially in superficial layers) is

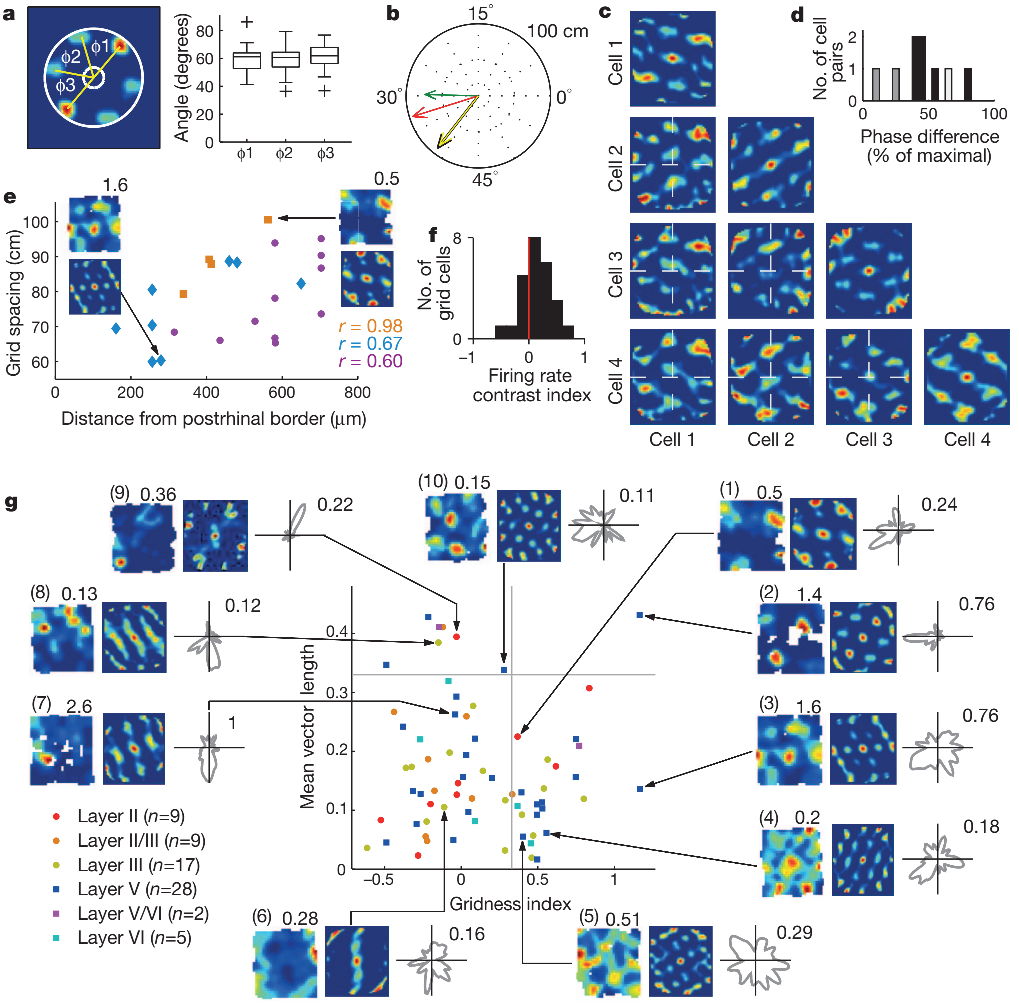

Figure 3 | Grid-cell properties in the bat resemble those in the rat. a, Left: definition of the three hexagon angles, depicted on the autocorrelogram annulus of a grid cell. Right: distribution of angles ($n = 25$ grid cells). Box plots show the median angles and interquartile and total ranges; +, outliers. **b**, Polar plot (60° cycle) showing four co-localized grid cells recorded simultaneously on the same tetrode in the superficial layers of MEC, depicting grid spacing (arrow length, cm) and orientation (angle within 60° cycle). Red, green, black and yellow arrows denote these four co-localized grid cells. **c**, Autocorrelograms (diagonal panels) and cross-correlograms (off-diagonal) of the four simultaneously recorded grid cells from **b**. **d**, Distribution of phase differences between pairs of co-localized grid cells. Different shading indicates different recording sites. **e**, Grid spacing increases with distance from postrhinal (dorsal) border of MEC. Colours of dots indicate individual bats and match the colours of r values. Insets show firing-rate maps and autocorrelograms of two grid cells recorded at different distances from the postrhinal border. **f**, Distribution of firing-rate contrast indexes for high versus low movement velocity. **g**, Scatter plot of mean vector length index versus gridness index for all neurons from MEC ($n = 70$). Colour and shape of symbols denote recording layer in MEC. Vertical and horizontal lines indicate 95th percentile of shuffled distributions of gridness and mean vector length, respectively. Insets show examples of neurons discussed in the main text, showing (from left to right) the rate map, spatial autocorrelogram and head-direction polar rate plots (grey). Peak firing rate (in Hz) is indicated for rate maps and polar maps.

theta-modulated[6], and they have similar phases[28], we also examined the temporal periodicity of the multi-unit activity, where firing rates are much higher than in individual neurons, and hence oscillations might be detected more robustly. We found that 100% of multi-unit sites where grid cells were recorded (17 out of 17) did not exhibit theta-modulated firing (Fig. 4h, right; theta index 0.97 ± 0.56; maximal value 2.1; see also Supplementary Figs 15–17). Fifth, because rat MEC neurons are often locked to a specific phase of the theta cycle[14,27,28], we examined whether spikes are locked to bats' theta phase during theta bouts. We found that bat MEC neurons indeed exhibited a clear, albeit weak, phase-locking during theta bouts (Fig. 4i, bottom, grey; see also Supplementary Fig. 18). Importantly, no phase locking could be observed outside the theta bouts (Fig. 4i, red). The contrast between phase locking of spikes during theta bouts versus lack of locking outside the bouts (Fig. 4i) indicates that theta bouts in bats are truly discrete and locally generated events. Sixth, to examine the possible contribution of theta bouts to grid formation, we removed in each grid cell all theta-bout epochs, and re-computed the firing-rate maps and two-dimensional autocorrelograms; this did not cause substantial alterations in the grid pattern (Fig. 4j, k and Supplementary Fig. 19). Notably, only a minority of spikes emitted by any single grid cell occurred during theta bouts (4.4 ± 0.75%). In fact, in some grid cells, the grid field existed in the absence of any spikes emitted during theta bouts (Fig. 4k, right; zero spikes emitted during all the theta bouts). Population analysis confirmed that theta-bout removal did not lead to significant changes in gridness values, in any of the grid cells (Fig. 4l, 100% of the cells showed changes in gridness that did not exceed the 95% confidence intervals). This suggests that the grids are maintained during times when theta oscillations are not present.

Taken together, these findings provide the first report on grid cells in a non-rodent species, which supports the generality of the grid-cell phenomenon across mammals; more importantly, our findings causally dissociate the link between the existence of grids and the existence of continuous theta-band oscillations in the mammalian entorhinal

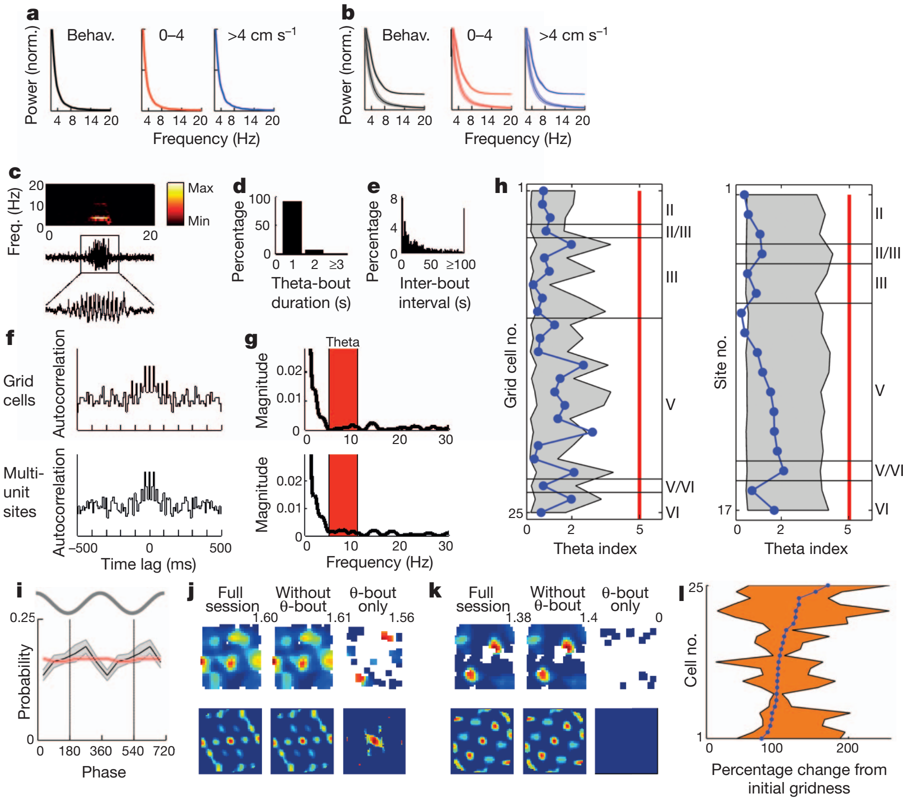

Figure 4 | No continuous theta oscillations in bat MEC. **a**, LFP power spectrum during a single behavioural session (left, Behav.), and separated according to bat's velocity (coloured panels). **b**, Population average LFP power spectrum for all behavioural sessions in which grid cells were recorded (left, Behav.), and separated by velocity (coloured panels). The two lines in each panel show the two reference types used for electrophysiological recordings: single-ended (ground screw, top line) and double-ended (local reference tetrode, bottom); vertical separation is for display purposes only (mean ± s.e.m.). Note the absence of a peak at theta frequency. **c**, LFP trace showing an example theta bout during locomotion. Middle 20-s wideband trace (1–475 Hz). The box around the theta bout serves as calibration bars: 7-s horizontal and 0.4-mV vertical. Bottom: 7-s zoom in. Top: spectrogram. **d**, Distribution of theta-bout durations during behaviour. **e**, Distribution of inter-bout intervals during behaviour. **f**, Spike-train temporal autocorrelograms for a single grid cell (top) and the multi-unit activity recorded at the same site (bottom). Bin size, 10 ms. **g**, Power spectrum of the autocorrelograms in **f**. Note the absence of spectral peak at the theta frequency range (5–11 Hz, highlighted in red). **h**, Theta indexes for grid cells ($n = 25$, left) and multi-unit sites in which grid cells were recorded ($n = 17$, right), arranged by recording layer in MEC (layer number indicated on the right). Shaded area indicates 95% confidence intervals. Notably, 96% (24 out of 25) of grid cells and 100% (17 of 17) of multi-unit sites did not show significant theta modulation, irrespective of the recording layer. **i**, Population average phase histograms of MEC neurons' discharge probability during theta bouts (grey curve) and during non-theta epochs (red). Both curves show mean ± s.e.m. Two theta cycles are shown for visualization purposes. **j**, **k**, Removal of theta bouts: rate maps (top) and spatial autocorrelograms (bottom) of two grid cells (**j** and **k**), for all the data (left), without theta bouts (middle) and during theta bouts only (right). Colour scale of rate maps normalized to maximal firing rate for all three maps for each neuron. **l**, Changes in gridness after theta-bout removal; data for all grid cells (blue dots, sorted) and 95% bootstrap confidence interval (orange area; Supplementary Information) are shown. None of the grid cells showed significant changes in gridness after removal of theta bouts.

cortex. The similarities in the anatomy and grid-cell properties between bats and rats strongly suggest that similar underlying neural mechanisms generate the grid, indicating that the functional dissociation between theta and grids generalizes across mammalian species. Although it is possible that continuous theta oscillations would be found in bats during flight, we emphasize that, under the specific crawling conditions of our experiments, we observed simultaneously the existence of grids without continuous theta oscillations in the LFP or in the spiking activity, which strongly argues against the theta-based class of computational models of grid cells[10–13], but is consistent with the other models which do not rely on theta oscillations[7–9].

Recently, two studies showed that inactivation of medial septum inputs to rat MEC disrupts grid fields, and also disrupts theta oscillations in MEC[28,29]. Additionally, these studies found that, after medial septum inactivation, the firing rates of MEC grid cells dropped by >40%, on average, and in many cases the firing rates dropped threefold and even fivefold[28,29]. These observations have been interpreted as supporting the oscillatory interference models[28,29], but they equally well support network models of grid cells: it is well known in the theory of neural networks that the removal of a major input to a network, if accompanied by a marked decrease in firing rates, can drive the network into a very different activity regime[30], which could disrupt grid formation. Thus, inactivation of a major input to a brain network[28,29] cannot serve to dissociate oscillation-based models from network models. In contrast, our study in bats did not manipulate the inputs to the entorhinal network, and thus provided a unique opportunity to causally challenge the oscillatory interference models of grid cells. More generally, we provide here a rare example of causally disproving a major class of computational models of a higher brain area.

METHODS SUMMARY

Immunohistochemical stainings were conducted to delineate the anatomical location and borders of the medial entorhinal cortex (MEC) in Egyptian fruit bats (*Rousettus aegyptiacus*). Single neuron activity and local field potentials (LFP) were recorded from hippocampal area CA1 and MEC of five bats (two and three bats, respectively), using tetrodes[17–19]. Neuronal activity and positional data were collected while bats foraged in a large arena (117 × 117 cm) in search of food. Place cells[19] in CA1 were identified using a criterion of spatial information >0.5 bits per spike (ref. 17). Grid cells and head-direction cells were identified using a standard gridness index[2] and mean vector length index of the head-direction tuning[4,5]; significance of these two indices was tested using a random shuffling procedure similar to that described previously in rats[4,5]. To quantify grid properties, we computed grid spacing, orientation, phase and velocity-modulation of the cell's firing[1,2]. High-frequency ripple oscillations in the LFP during sleep were detected as transients in the power of the filtered LFP trace (80–160 Hz) exceeding 7 s.d. above the mean power[17]. Theta oscillation epochs were defined as 2-s windows in which the ratio between the power in the theta (4–8 Hz) and delta (2–4 Hz) frequency ranges exceeded 2.0. Theta modulation of neuronal firing was assessed using a standard theta index, which is based on the spectral power of the spike train temporal autocorrelogram[4–6]. Detailed experimental and analytical procedures are provided in the Supplementary Information.

Received 9 April; accepted 27 September 2011.

1. Hafting, T., Fyhn, M., Molden, S., Moser, M.-B. & Moser, E. I. Microstructure of a spatial map in the entorhinal cortex. *Nature* **436,** 801–806 (2005).
2. Sargolini, F. *et al.* Conjunctive representation of position, direction, and velocity in entorhinal cortex. *Science* **312,** 758–762 (2006).
3. Barry, C., Hayman, R., Burgess, N. & Jeffery, K. J. Experience-dependent rescaling of entorhinal grids. *Nature Neurosci.* **10,** 682–684 (2007).
4. Langston, R. F. *et al.* Development of the spatial representation system in the rat. *Science* **328,** 1576–1580 (2010).
5. Wills, T. J., Cacucci, F., Burgess, N. & O'Keefe, J. Development of the hippocampal cognitive map in preweanling rats. *Science* **328,** 1573–1576 (2010).
6. Boccara, C. N. *et al.* Grid cells in pre- and parasubiculum. *Nature Neurosci.* **13,** 987–994 (2010).
7. Fuhs, M. C. & Touretzky, D. S. A spin glass model of path integration in rat medial entorhinal cortex. *J. Neurosci.* **26,** 4266–4276 (2006).
8. McNaughton, B. L., Battaglia, F. P., Jensen, O., Moser, E. I. & Moser, M.-B. Path integration and the neural basis of the 'cognitive map'. *Nature Rev. Neurosci.* **7,** 663–678 (2006).
9. Burak, Y. & Fiete, I. R. Accurate path integration in continuous attractor network models of grid cells. *PLOS Comput. Biol.* **5,** e1000291 (2009).
10. Burgess, N., Barry, C. & O'Keefe, J. An oscillatory interference model of grid cell firing. *Hippocampus* **17,** 801–812 (2007).
11. Giocomo, L. M., Zilli, E. A., Fransén, E. & Hasselmo, M. E. Temporal frequency of subthreshold oscillations scales with entorhinal grid cell field spacing. *Science* **315,** 1719–1722 (2007).
12. Hasselmo, M. E., Giocomo, L. M. & Zilli, E. A. Grid cell firing may arise from interference of theta frequency membrane potential oscillations in single neurons. *Hippocampus* **17,** 1252–1271 (2007).
13. Blair, H. T., Welday, A. C. & Zhang, K. Scale-invariant memory representations emerge from Moiré interference between grid fields that produce theta oscillations: a computational model. *J. Neurosci.* **27,** 3211–3229 (2007).
14. Hafting, T., Fyhn, M., Bonnevie, T., Moser, M.-B. & Moser, E. I. Hippocampus-independent phase precession in entorhinal grid cells. *Nature* **453,** 1248–1252 (2008).
15. Yovel, Y., Falk, B., Moss, C. F. & Ulanovsky, N. Optimal localization by pointing off axis. *Science* **327,** 701–704 (2010).
16. Ulanovsky, N. & Moss, C. F. What the bat's voice tells the bat's brain. *Proc. Natl Acad. Sci. USA* **105,** 8491–8498 (2008).
17. Ulanovsky, N. & Moss, C. F. Hippocampal cellular and network activity in freely moving echolocating bats. *Nature Neurosci.* **10,** 224–233 (2007).
18. Ulanovsky, N. & Moss, C. F. Dynamics of hippocampal spatial representation in echolocating bats. *Hippocampus* **21,** 150–161 (2011).
19. Wilson, M. A. & McNaughton, B. L. Dynamics of the hippocampal ensemble code for space. *Science* **261,** 1055–1058 (1993).
20. Chrobak, J. J. & Buzsáki, G. High-frequency oscillations in the output networks of the hippocampal-entorhinal axis of the freely behaving rat. *J. Neurosci.* **16,** 3056–3066 (1996).
21. Buzsáki, G. Theta oscillations in the hippocampus. *Neuron* **33,** 325–340 (2002).
22. Stewart, M. & Fox, S. E. Hippocampal theta activity in monkeys. *Brain Res.* **538,** 59–63 (1991).
23. Ekstrom, A. D. *et al.* Human hippocampal theta activity during virtual navigation. *Hippocampus* **15,** 881–889 (2005).
24. Witter, M. P., Wouterlood, F. G., Naber, P. A. & Van Haeften, T. Anatomical organization of the parahippocampal-hippocampal network. *Ann. NY Acad. Sci.* **911,** 1–24 (2000).
25. Solstad, T., Boccara, C. N., Kropff, E., Moser, M.-B. & Moser, E. I. Representation of geometric borders in the entorhinal cortex. *Science* **322,** 1865–1868 (2008).
26. Deshmukh, S. S., Yoganarasimha, D., Voicu, H. & Knierim, J. J. Theta modulation in the medial and the lateral entorhinal cortices. *J. Neurophysiol.* **104,** 994–1006 (2010).
27. Mizuseki, K., Sirota, A., Pastalkova, E. & Buzsáki, G. Theta oscillations provide temporal windows for local circuit computation in the entorhinal-hippocampal loop. *Neuron* **64,** 267–280 (2009).
28. Brandon, M. P. *et al.* Reduction of theta rhythm dissociates grid cell spatial periodicity from directional tuning. *Science* **332,** 595–599 (2011).
29. Koenig, J., Linder, A. N., Leutgeb, J. K. & Leutgeb, S. The spatial periodicity of grid cells is not sustained during reduced theta oscillations. *Science* **332,** 592–595 (2011).
30. Hansel, D. & Sompolinsky, H. Modeling feature selectivity in local cortical circuits. In *Methods in Neuronal Modeling: from Synapses to Networks* 2nd edn (eds Kock, C. & Segev, I.) 499–567 (MIT Press, 1998).

Supplementary Information is linked to the online version of the paper at www.nature.com/nature.

Acknowledgements We thank D. Derdikman, S. Romani, M. Ahrens and Y. Cohen for comments on the manuscript, M. Melcón for initial assistance with hippocampal CA1 recordings, M. Weinberg for veterinary oversight, and R. Eilam and C. Ra'anan for histology. This study was supported by research grants from the Israel Science Foundation and Minerva Foundation to N.U., by a Lev-Zion predoctoral excellence fellowship to M.M.Y., as well as by grants from the Norwegian Research Council and the Kavli Foundation to M.P.W.

Author Contributions M.M.Y. and N.U. designed the study, conducted the experiments, analysed the data and wrote the manuscript. M.P.W. performed immunohistochemical analyses, delineated the anatomical structures in the hippocampus and entorhinal cortex of Egyptian fruit bats, and verified recording sites. All authors discussed the results and commented on the manuscript.

Author Information Reprints and permissions information is available at www.nature.com/reprints. The authors declare no competing financial interests. Readers are welcome to comment on the online version of this article at www.nature.com/nature. Correspondence and requests for materials should be addressed to N.U. (nachum.ulanovsky@weizmann.ac.il).

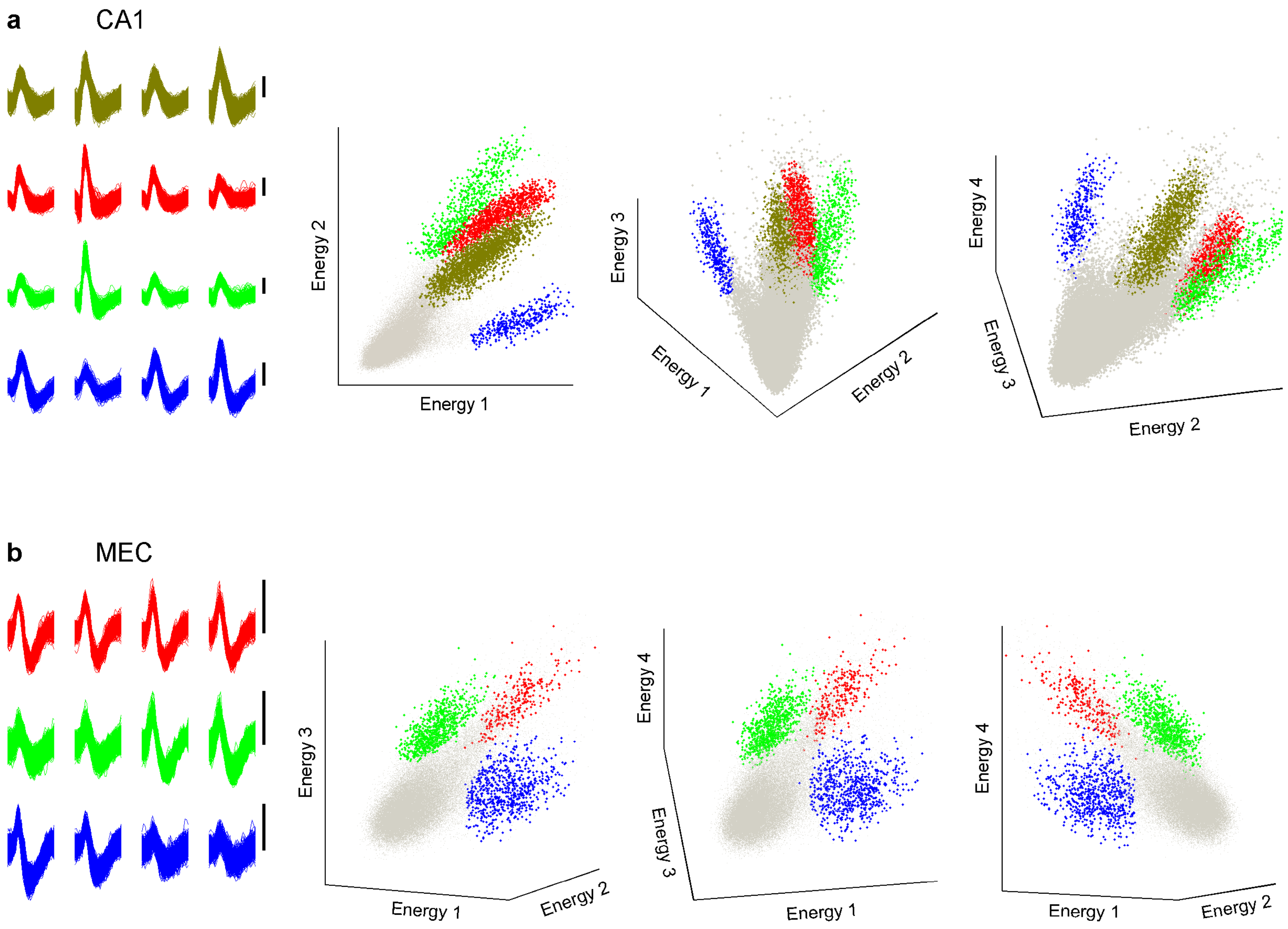

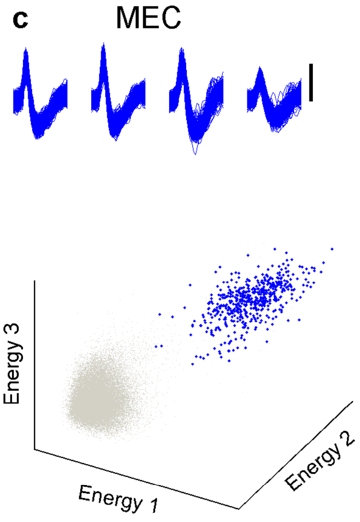

Supplementary Figure 1 | Examples of spike sorting in hippocampal area CA1 and in MEC. **a,** Spike sorting in CA1. Left, waveforms of four neurons (different colors, rows) recorded simultaneously on a single tetrode (four channels, columns) in dorsal CA1. Data are from all three sessions of one day (all spikes are superimposed). Scale bar, 100 µV; waveform duration, 1-ms. Right, three-dimensional views of the projections of spike energies of the recorded CA1 neurons; colors match the waveforms on the left. **b,** Spike sorting in MEC. Left, waveforms of three neurons (rows) recorded simultaneously on one tetrode in layer V of the bat MEC; same notation as in **a**. Right, three-dimensional projections of the spike energies of the recorded MEC cells; colors match the waveforms on the left. **c,** Another example of a single unit recorded in MEC layer V. Shown are the waveforms (top) and a single three-dimensional view of the projections of spike energies (bottom) for this neuron.

Supplementary Figure 2

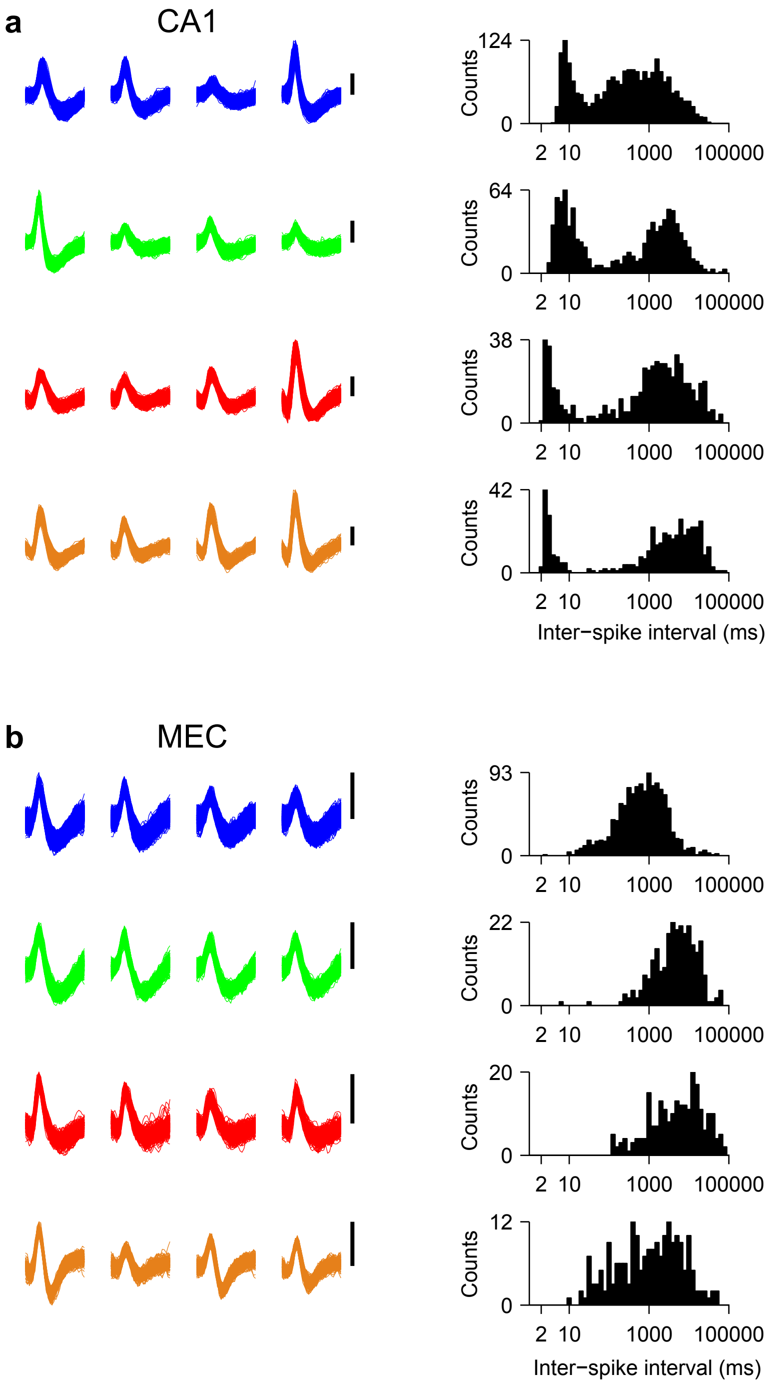

Supplementary Figure 2 | Inter-spike interval distributions for hippocampal CA1 and MEC neurons. Waveforms (left) and inter-spike interval histograms (right) of four example CA1 neurons (**a,** four rows) and 4 MEC neurons (**b,** four rows). The CA1 neurons were recorded in 4 different recording locations from two bats; the MEC neurons were recorded on 3 different days from 4 different recording locations from two different bats. Note the bimodality of the inter-spike interval distributions in CA1, with a peak at small inter-spike intervals – suggesting pronounced complex-spike bursts, as expected from hippocampal CA1 pyramidal cells. In contrast, the MEC neurons exhibited a unimodal distribution of inter-spike intervals, indicating the lack of pronounced bursting. Scale bars on left, 100 μV; waveform duration, 1-ms.

Supplementary Figure 3

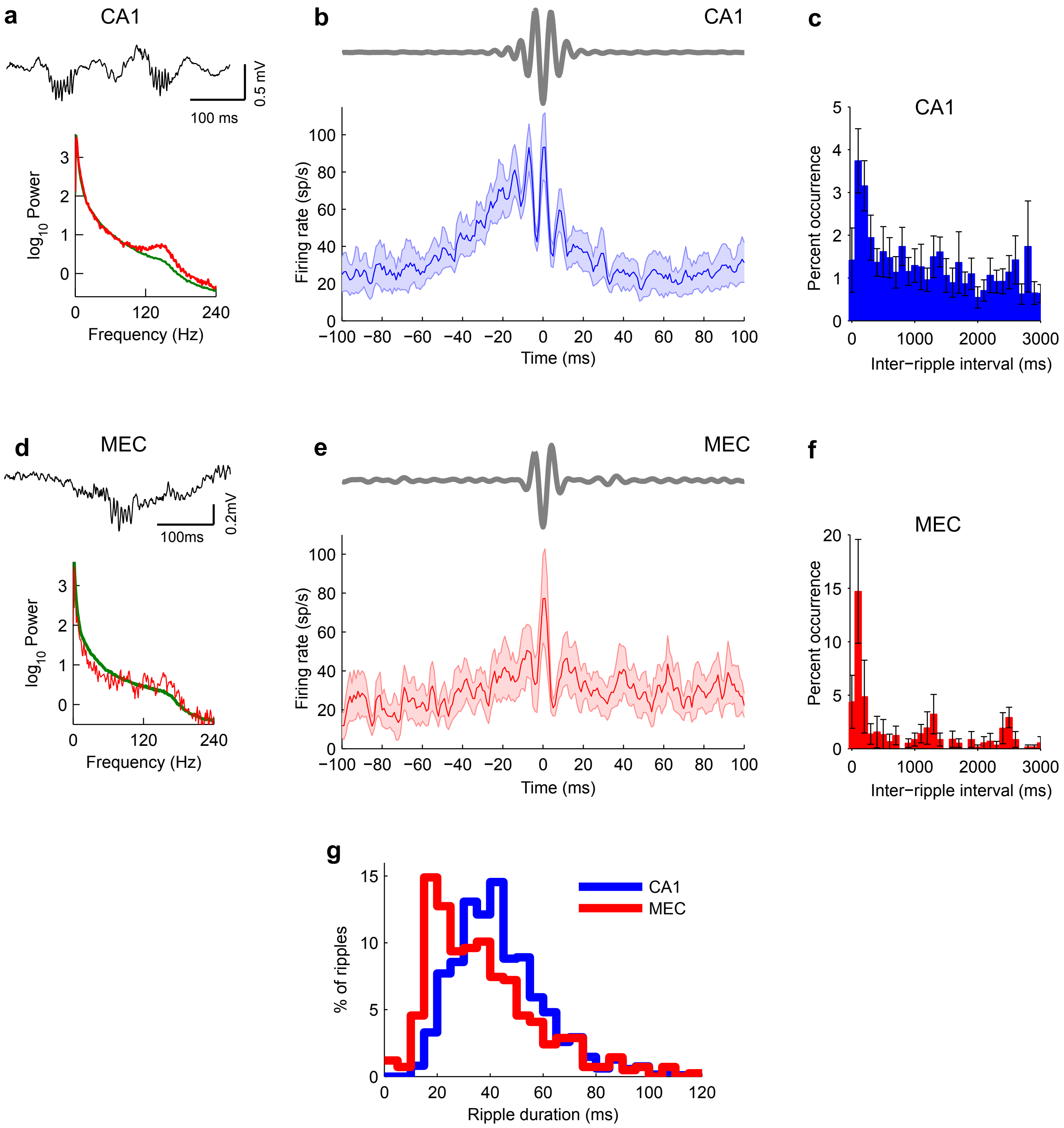

Supplementary Figure 3 | Properties of ripples in bat CA1 and MEC. a, d, Top, example LFP trace (wideband, 1–475 Hz) showing high-frequency ripples. Bottom: LFP power spectrum for all the sleep data from that day (green) and for 1-s segments extracted around identified ripples (red) in CA1 (**a**) or MEC (**d**). **b, e,** Average ripple waveform (top) and ripple-triggered multiunit firing rate (bottom, mean ± s.e.m) for all sites where place cells in CA1 (**b**) or grid cells in MEC (**e**) were recorded. Positivity is pointing upwards. Note the increase in population firing rate on the ripple trough (time 0), and the phase-locking of hippocampal firing to the ripple oscillatory cycles – similar to rodents[21,31]. **c, f,** Distribution of inter-ripple intervals over all recording sites (mean ± s.e.m) in CA1 (**c**) and MEC (**f**). Note the peak at short intervals for both CA1 and MEC ripples, suggesting that ripples often occurred in doublets, similar to rodents[31,32]. **g,** Distribution of ripple durations for CA1 (blue) and MEC (red). Ripples in CA1 tended to be longer than those in MEC, similar to the rat[32].

Supplementary Figure 4

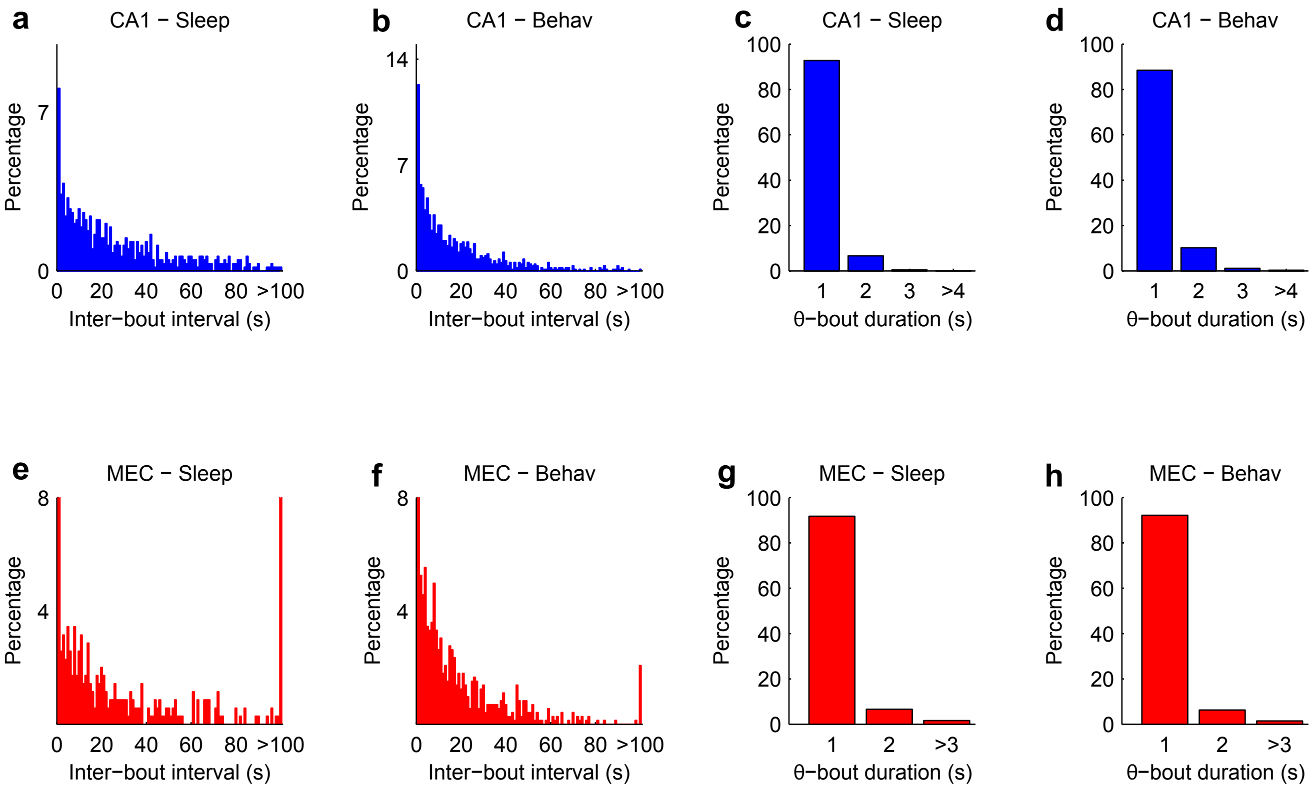

Supplementary Figure 4 | Theta bouts in CA1 and MEC. a, e, Distribution of inter-bout intervals during sleep in CA1 (**a**) and MEC (**e**). **b, f,** Distribution of inter-bout intervals during behavior in CA1 (**b**) and MEC (**f**). **c, g,** Distribution of theta-bout durations during sleep in CA1 (**c**) and MEC (**g**). **d, h,** Distribution of theta-bout durations during behavior in CA1 (**d**) and MEC (**h**). The histograms shown in panels **f** and **h** correspond to the histograms shown in Fig. 4e and Fig. 4d of the main text, respectively.

Supplementary Figure 5 - Page 1

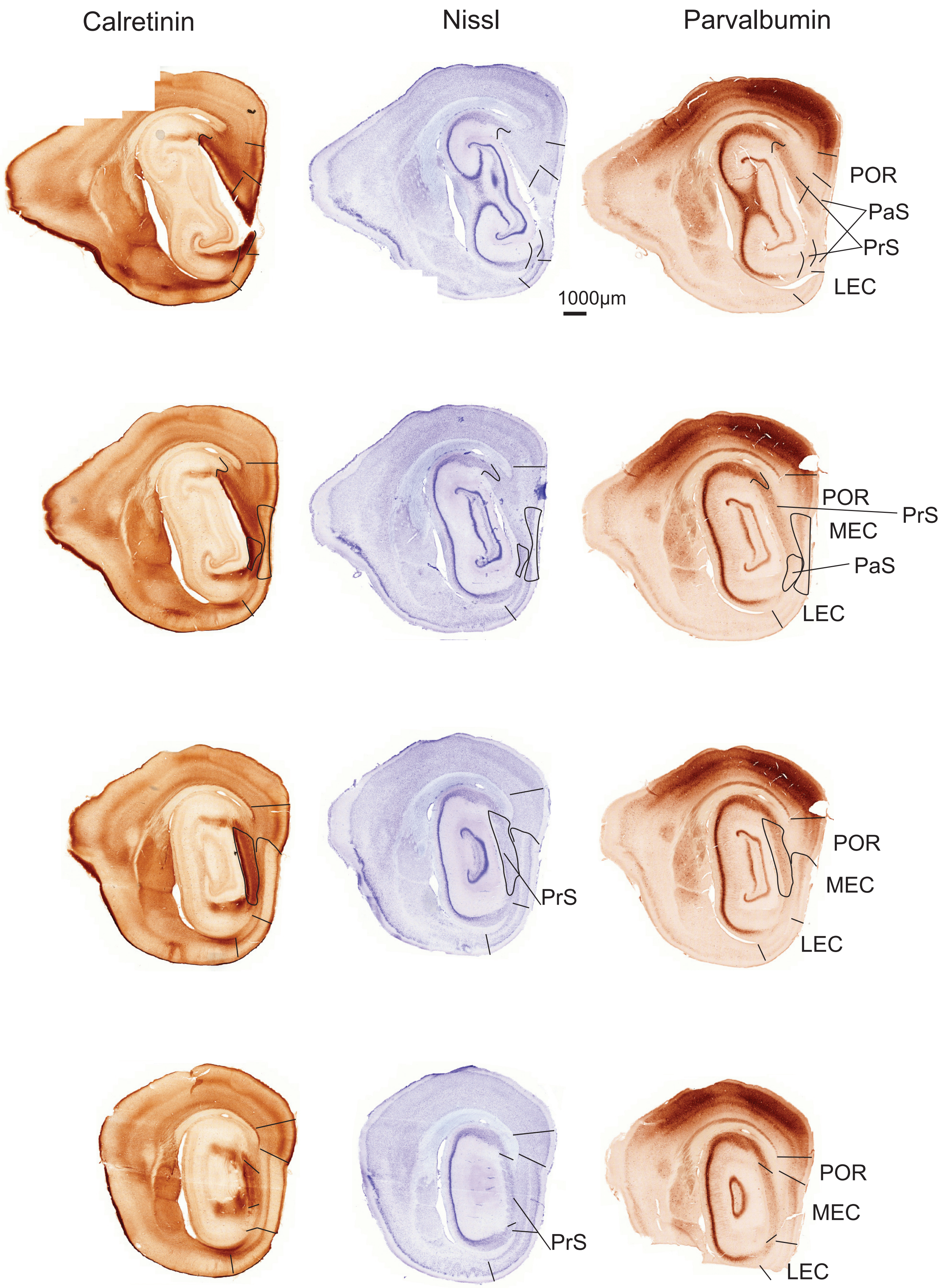

Supplementary Figure 5 - Page 2

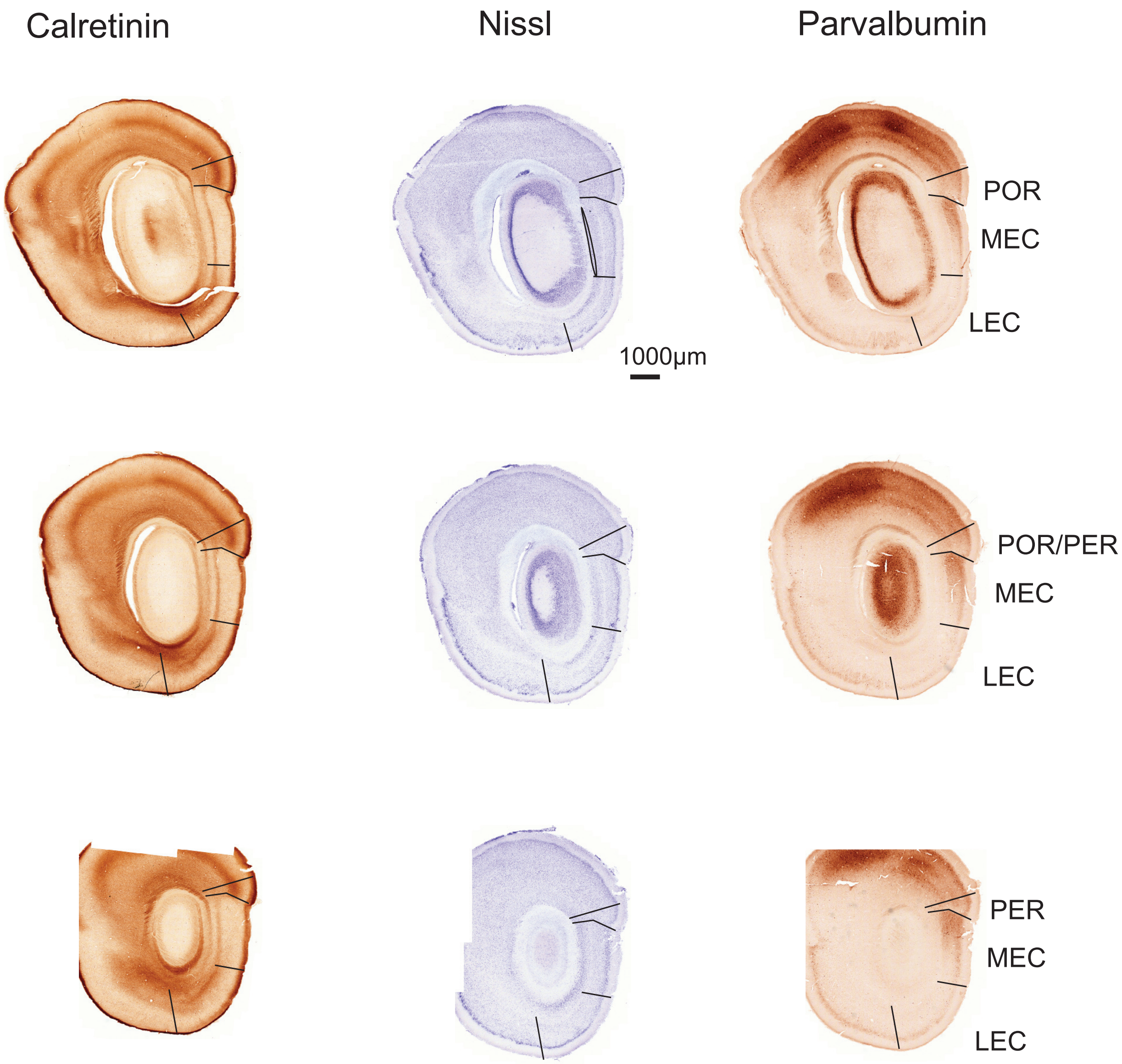

Supplementary Figure 5 | Anatomical delineation of MEC and adjacent brain structures in the bat. Sagittal sections stained with calretinin (left), Nissl (middle) and parvalbumin (right), arranged from medial (top row of page 1) to lateral (bottom row of page 2). All sections are from the same brain; each row shows three adjacent sections. Note the near absence of calretinin staining in bat MEC, contrasted with strong calretinin staining in postrhinal cortex (POR) and in the pre- and para-subiculum (PrS and PaS, respectively). These abrupt changes in staining pattern coincide with marked changes in cytoarchitectonic features such as cessation of the *lamina dissecans* which is prominent in MEC, and a change in cell sizes and packing density in layers II and III. Likewise, the borders between MEC and PrS and PaS are easily recognizable (see also Supplementary Fig. 6) and both patterns of changes are similar to that reported in the rat[33] (see also ref. 29). LEC, lateral entorhinal cortex.

Supplementary Figure 6

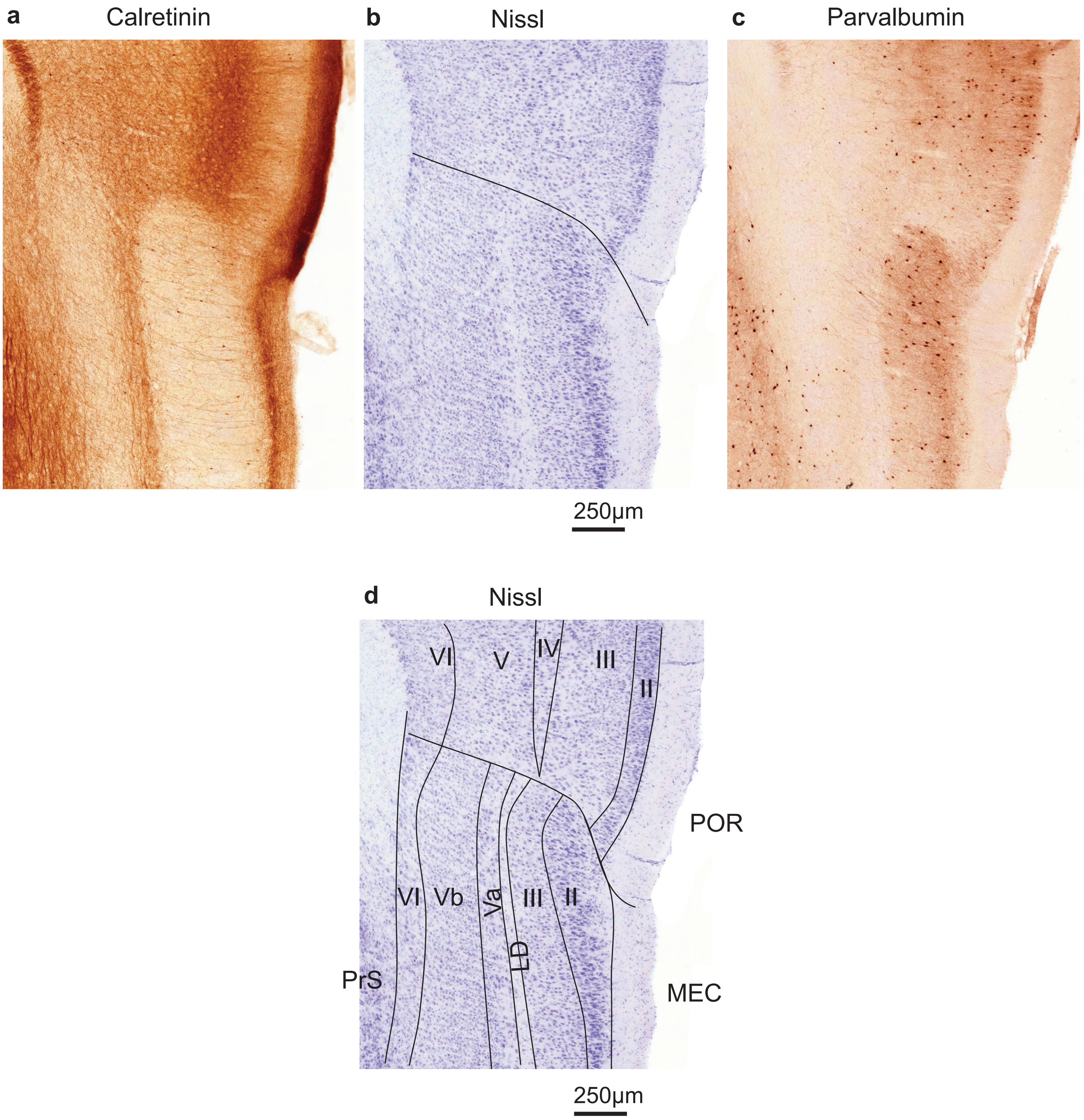

Supplementary Figure 6 | Anatomical delineation of the laminar structure of bat MEC and the location of MEC/postrhinal border. a–c, Higher-magnification pictures of 3 sagittal sections from Supplementary Fig. 5 (same sections as the bottom-most row on page 1 of supplementary Fig. 5), stained with calretinin (**a**), Nissl (**b**) and parvalbumin (**c**). Postrhinal (dorsal) border of bat MEC is marked in **b**. **d,** Delineation of the laminar structure of MEC and adjacent areas (same section as in b). Note the presence of a cell-body free layer (LD – *lamina dissecans*) in the MEC but not in the bordering postrhinal cortex (POR) – similar to the rat[33,34]. At the same level, there is a clear reduction in average cell size in layer II of postrhinal cortex (POR) compared to the large cell bodies in layer II of MEC, and the striking columnar organization of layer V of MEC is replaced by the more typical laminar organization seen in isocortex. The cytoarchitectonic border coincides with a near absence of calretinin staining in the bat MEC layers II, III, V and VI, but strong calretinin staining in POR, and an intense parvalbumin staining in MEC layers II and III, contrasted by the near absence of parvalbumin staining in the immediately adjacent portions of POR. This pattern of abrupt changes in cytoarchitectonic and chemoarchitectonic features is very similar to that observed in rats[33] (see also ref. 29), and it provides a precise indication of the MEC/postrhinal border. Note also the easily recognizable border between MEC and presubiculum (PrS).

Supplementary Figure 7

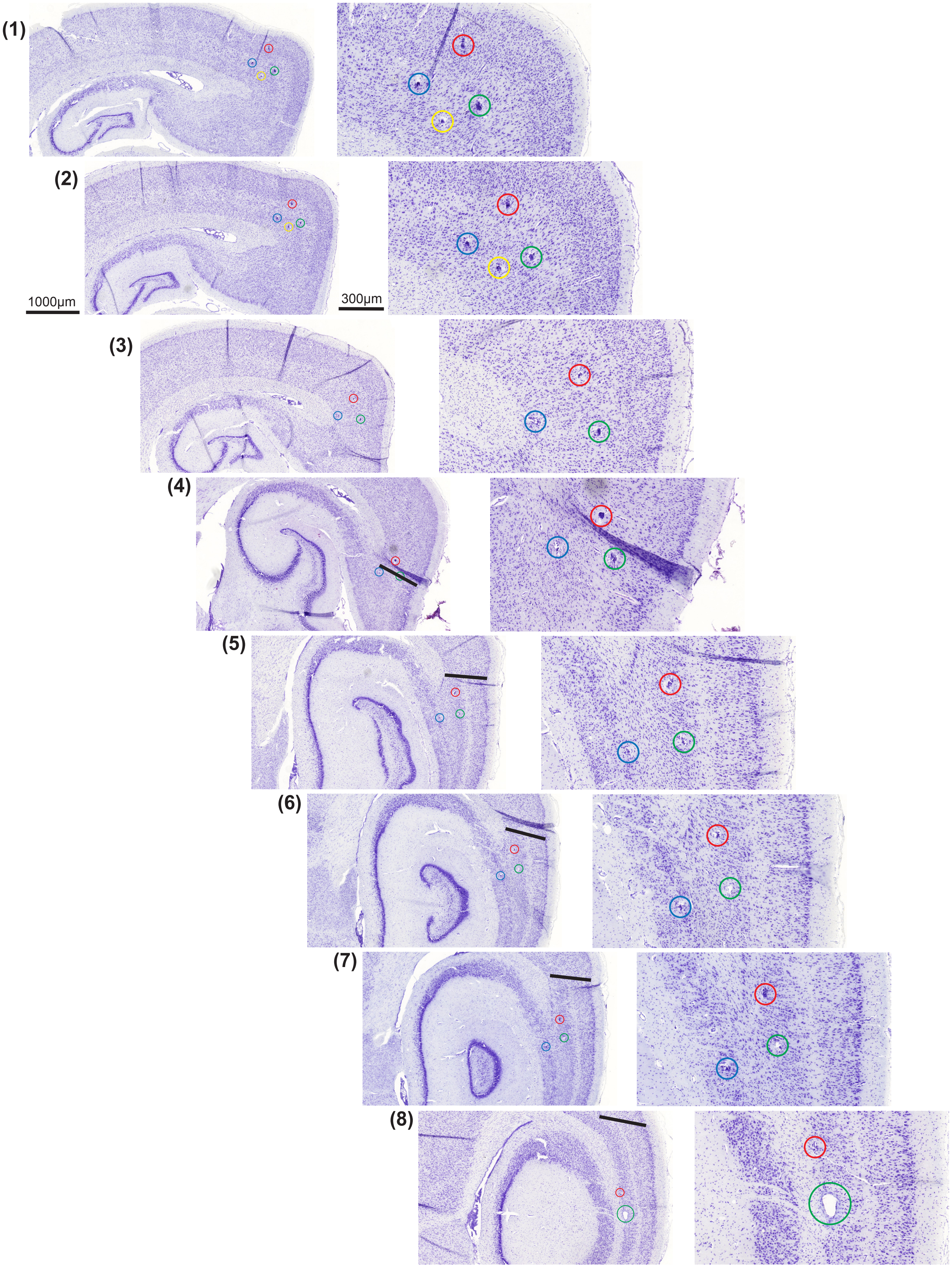

Continued from previous page

Supplementary Figure 7 | Example of the reconstruction of tetrode tracks aimed at the MEC of the bat. Eight Sagittal Nissl-stained sections from one experimental bat are arranged from medial (top) to lateral (bottom), and illustrate the anatomical reconstruction of 4 tetrode tracks in this bat (these were all the 4 tetrodes in our 4-tetrode microdrive). Left, wide-view; right, zoom-in on the region of the tetrode tracks. Postrhinal (dorsal) border of bat MEC is marked by a black line, wherever it was clearly visible. The combination of the angled penetration (see Supplementary Methods) and the Sagittal slicing of the brain, resulted in penetrations which are recognizable as little holes (sometimes surrounded by glial scar) that proceeded over many consecutive sections. Individual tetrode tracks are indicated here by different colored circles. Two tetrodes reached MEC, and on these two tetrodes we recorded grid cells (red and green tetrodes). One tetrode reached the presubiculum (blue), and one tetrode was used as reference and was left in the cortex above MEC (yellow). Sections #1–3 show the progression of all 4 tetrodes through cortex dorsal to MEC. Note that the tetrode track of our reference tetrode (yellow) ends in the cortex well above MEC, as it is still visible in section #2 but no longer visible in section #3. Section #4 shows the three tetrode tracks as they pass near the MEC border. Sections #5–7 show the progression of the tetrode tracks inside MEC (red and green tetrodes) and inside presubiculum (blue tetrode). At the end of the experiment, a lesion was made on the "green tetrode" (see also Supplementary Methods) and this lesion is visible in section #8 (see also Fig. 2b of the main text, which shows an adjacent section where this lesion is visible).

Supplementary Figure 8

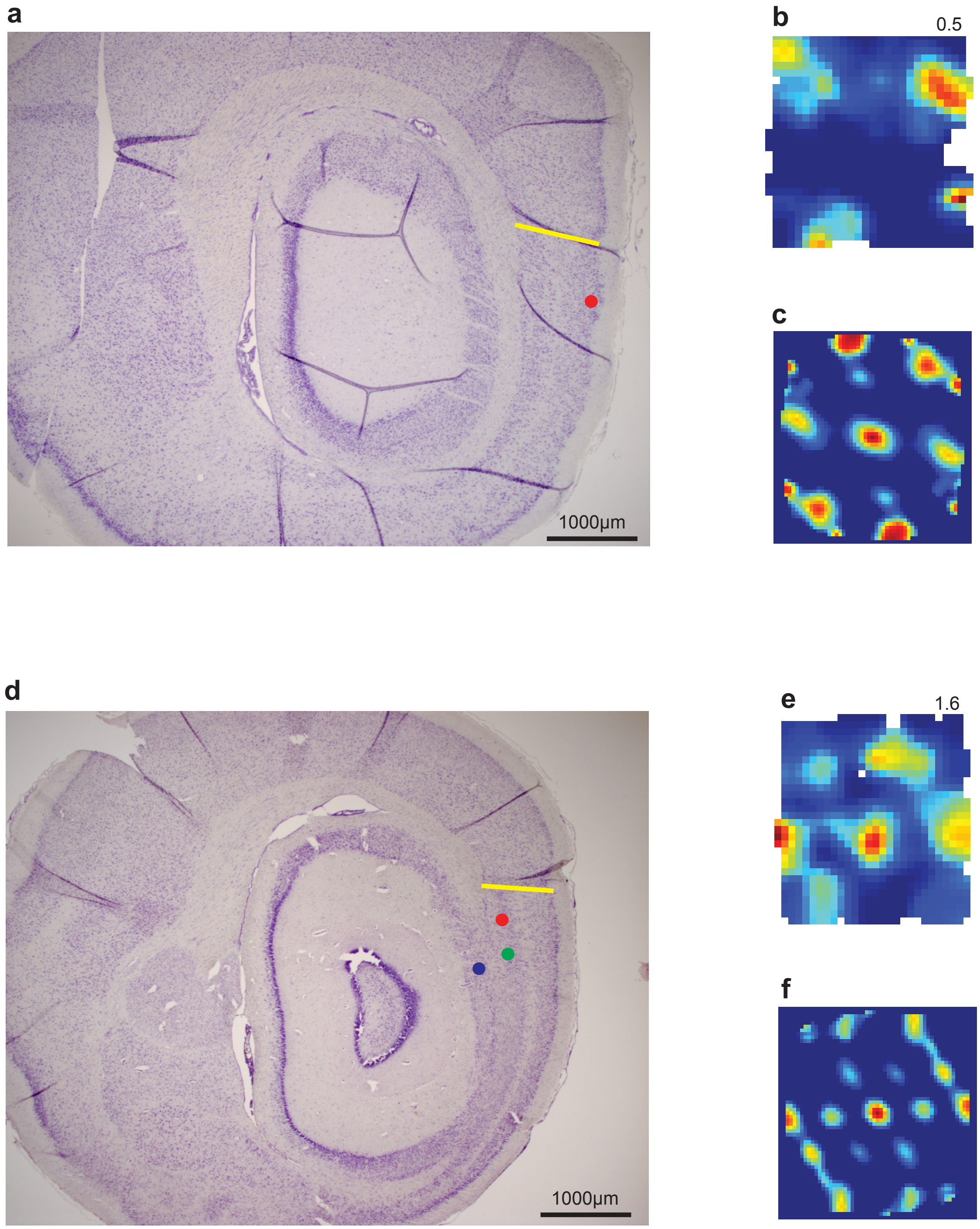

Supplementary Figure 8 | Examples of recording locations of grid-cells in bat MEC. **a,** Recording location in layer II (red dot). Yellow line, dorsal border of MEC (postrhinal border). **b, c,** Color coded rate map (**b**) and spatial autocorrelation (**c**) of a single grid-cell recorded at the location indicated by the red dot in **a**. **d,** Recording location of two tetrodes in MEC layer V (red and green dots) and one tetrode in presubiculum (blue dot). Yellow line, dorsal border of MEC. **e, f,** Rate map (**e**) and spatial autocorrelation (**f**) of a single grid-cell recorded at the location indicated by the red dot in **d** (same neuron as in Fig. 2c,f of the main text).

Supplementary Figure 9

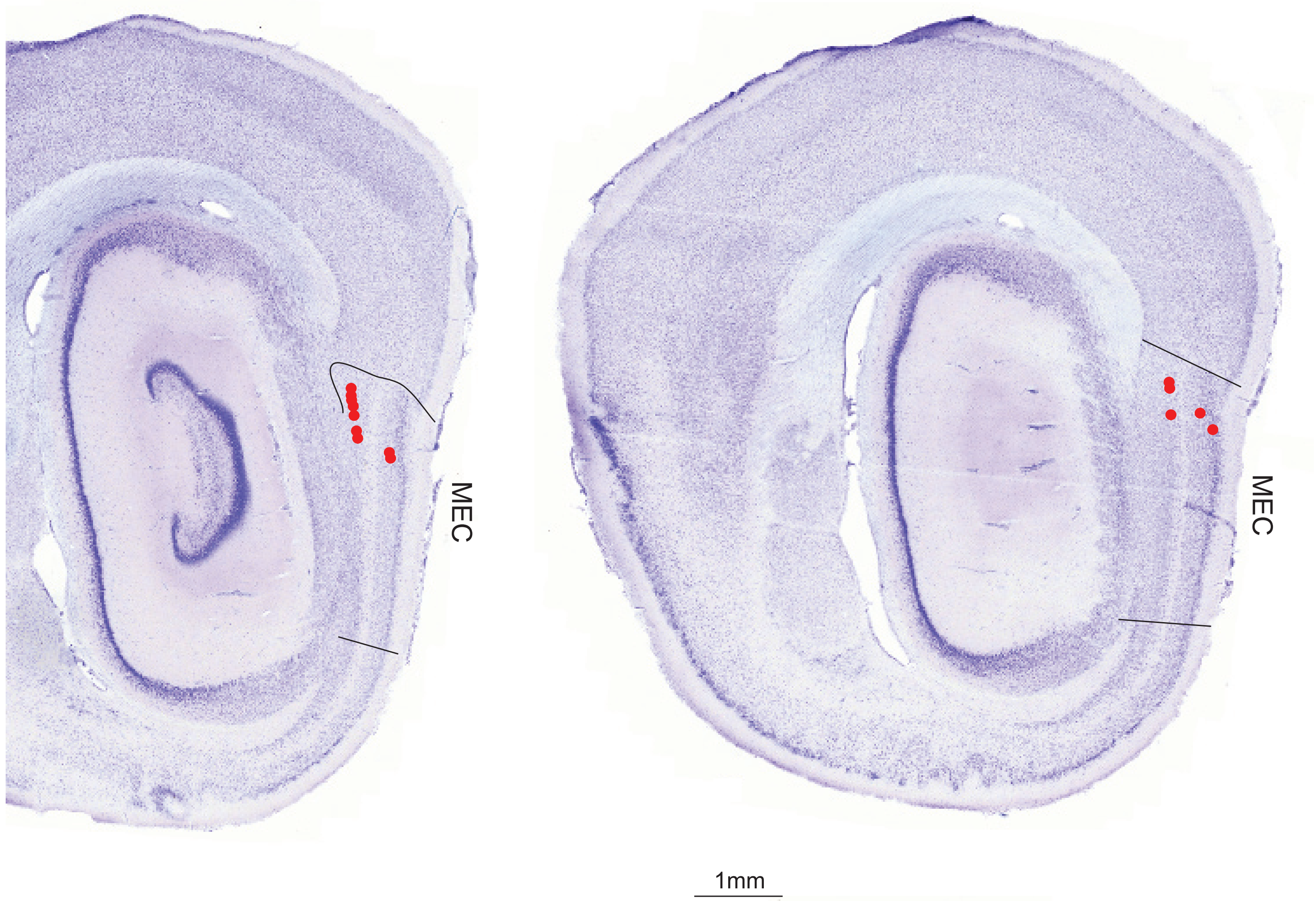

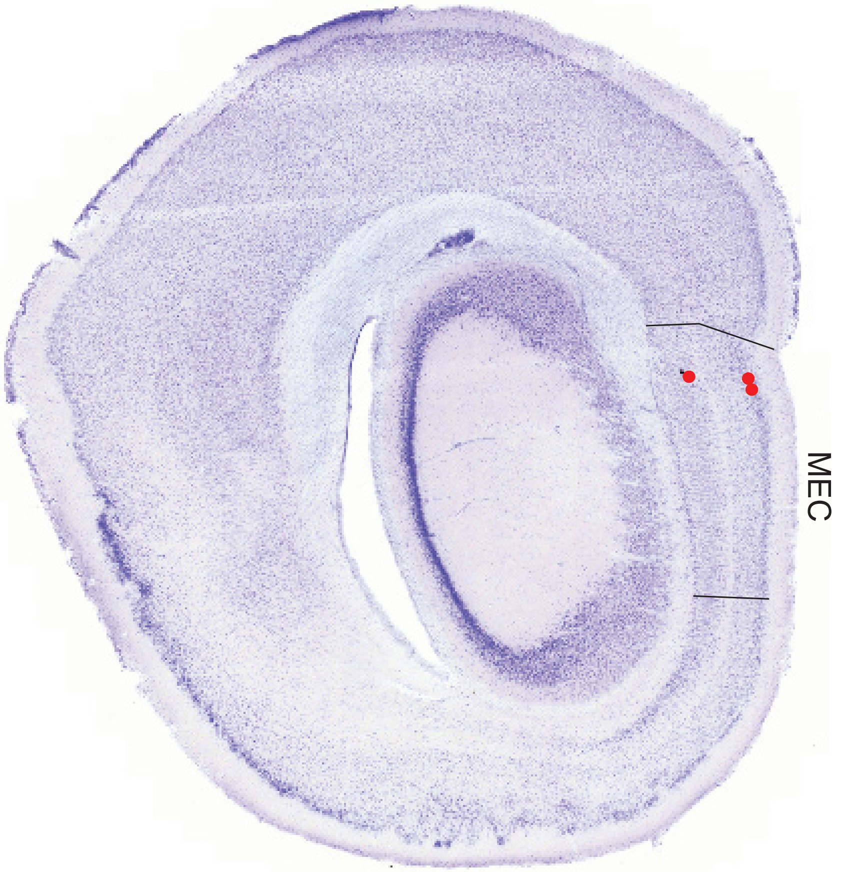

Supplementary Figure 9 | Recording locations of grid cells in the bat MEC. Recording locations of all the grid cells that we recorded from three bats are presented here on three standardized brain sections (17 recording locations, shown as 17 red dots). These three standardized sections are the same as the fully delineated sections presented in Supplementary Fig. 5 (bottom two rows of Page-1 and Top row on Page-2 of Supplementary Fig. 5). Black lines indicate the dorsal and ventral boundaries of MEC in the bat.

Supplementary Figure 10

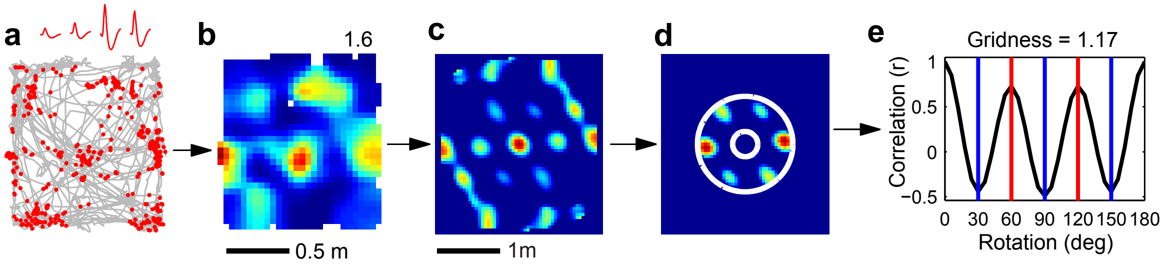

Supplementary Figure 10 | Computation of the gridness index. a, Trajectory of the bat (gray lines) with superimposed locations of action potentials (red dots) for a single neuron recorded from bat MEC (recording position indicated in Fig. 2c,d, and supplementary Fig. 8d). Average waveform shapes for this neuron are shown on top, for the 4 channels of the tetrode. **b,** Color-coded rate map, with the peak firing-rate indicated. **c,** Color-coded spatial autocorrelogram of the rate-map (see Supplementary Methods); the spatial scale in the autocorrelogram is double that in the original rate-map. **d,** An annulus is extracted such that it contains the 6 inner peaks of the hexagonal grid, with the central peak removed (Supplementary Methods). **e,** Correlation values are computed between rotated versions of the extracted annulus (in steps of 6°) and the original (un-rotated) annulus. Note the sinusoidal modulation of the correlation values, with maxima every 60°, as expected from a hexagonal shape. The gridness index is then derived as the difference between the minimal correlation value at 60° and 120° and the maximal correlation value at 30°, 90° and 150°.

Supplementary Figure 11

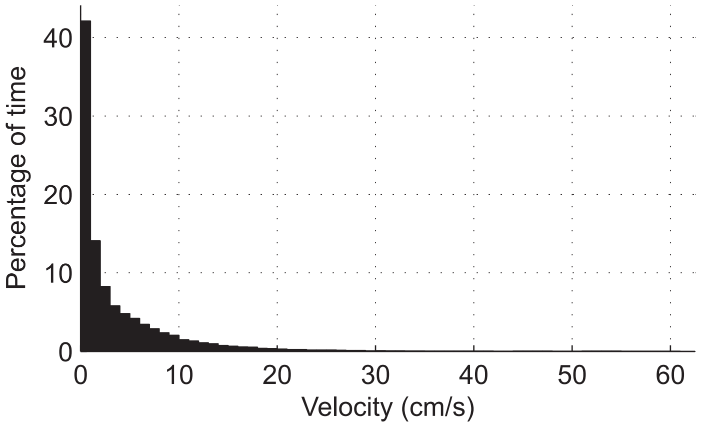

Supplementary Figure 11 | Bat crawling velocities. Distribution of the bats' crawling velocity, pooled across all bats from which recordings were made (5 bats, see Supplementary Methods). Mean velocity was 3.7 cm/s: Approximately 3 times slower than average running velocities observed in adult rats under similar experimental conditions, which are typically ~10 cm/s [14,19].

Supplementary Figure 12

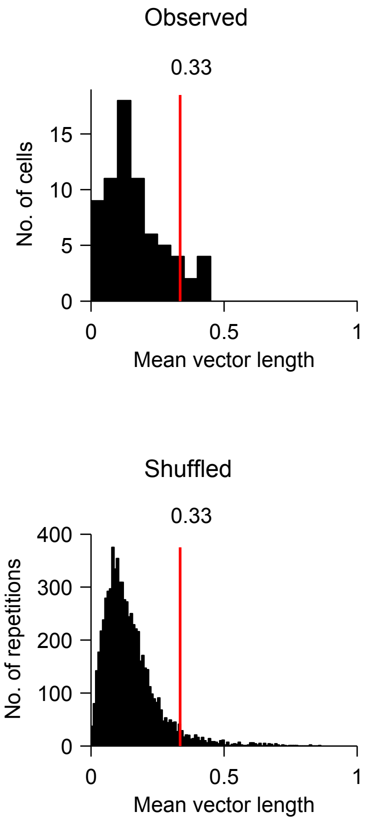

Supplementary Figure 12 | Observed and shuffled distributions of the mean vector length. The mean vector length is a standard measure of the directionality of the head-direction tuning curve of a neuron[13,14,19,27,35]. Shown is the distribution of the mean vector length for all MEC neurons (top, 'observed') and for the shuffled data (bottom, 'shuffled'). See Supplementary Methods for details of shuffling procedure. Red line and number indicate the 95th percentile of the shuffled distribution, which was subsequently used as threshold. Neurons which had a mean vector length value that exceeded this threshold were defined as head direction cells. Bin size, 0.05. Note that the threshold here (mean vector length = 0.3349) happened to have a similar numerical value as the threshold for the gridness (gridness = 0.3320, Fig. 2h); this is a coincidence, as these two indexes are generally not related.

Supplementary Figure 13

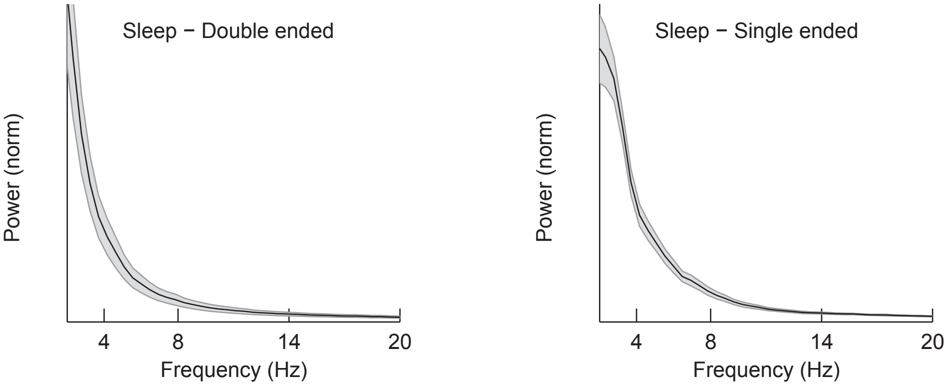

Supplementary Figure 13 | LFP theta oscillations in MEC during sleep. Population average spectral power of LFP (normalized to power at 2-Hz) for all sleep sessions, across all MEC bats (mean ± s.e.m. over all the sessions). Left, double-ended LFP recordings (using as reference a tetrode located outside MEC). Right, single-ended LFP recordings (using as reference the ground-screw in the skull's frontal plate). Note the absence of a peak at the theta frequency range in both cases.

Supplementary Figure 14

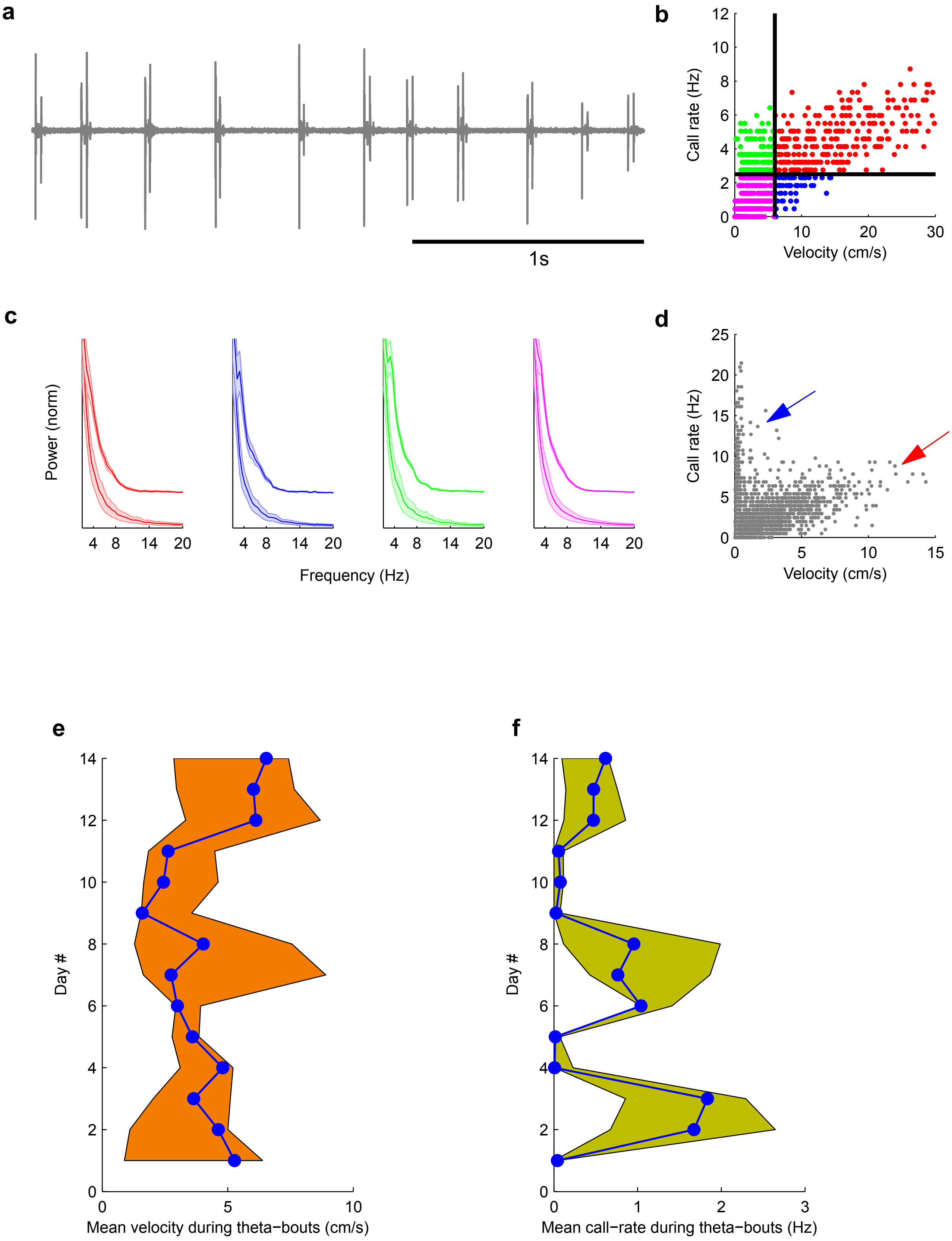

Continued from previous page

Supplementary Figure 14 | Relationships between the echolocation rate and crawling velocity of the bat, and the LFP in bat MEC. For testing how the bat's echolocation call-rate and movement velocity affect theta oscillations in the LFP, we arbitrarily defined 4 behavioral modes: low velocity and low echolocation rate; low velocity and high echolocation rate; high velocity and low echolocation rate; high velocity and high echolocation rate. The threshold between 'high' and 'low' velocity was set to 6 cm/s, and the threshold between high and low rate of echolocation calls was set to 2.5 Hz. The LFP recorded in MEC was segmented separately for each of these 4 behavioral modes, and the corresponding average power spectra were computed. **a,** Representative 3-s audio trace recorded during behavior, showing the echolocation double-clicks of the Egyptian fruit bat. Sonar signals were heterodyned down from their original 35-kHz frequency to 4-kHz, to facilitate recordings (see Supplementary Methods). Scale bar, 1-s. **b,** Echolocation call rate (y-axis) versus movement velocity (x-axis). Data are from a single behavioral session. Black horizontal and vertical lines are the thresholds (velocity = 6 cm/s, call rate = 2.5 Hz) used to define the 4 behavioral modes: Low velocity and low call rate (magenta), low velocity and high call rate (green), high velocity and low call rate (blue), high velocity and high call rate (red). Note the nearly linear relation between the sonar call-rate and velocity. **c,** Population average spectral power of LFP (normalized to power at 2-Hz) computed for each behavioral mode (colors matched to panel b) and presented for double-ended recordings (bottom traces) and for single-ended recordings (top traces; shifted vertically for display purposes only). Data are presented as mean ± s.e.m. Note the lack of a spectral peak at the theta frequency range in all cases. **d,** Comparison to the behavior of big brown bats[4], the hippocampus of which we previously studied[4,5]: Plotted is the echolocation call rate (y-axis) versus movement velocity (x-axis) for the big brown bat. Note the presence of two prominent behavioral modes in this bat species, one characterized by relatively high velocity and high call-rate, which are correlated to each other (red arrow) – similar to the data from the Egyptian fruit bat (panel b here) – and another behavioral mode characterized by low velocities and high echolocation rate (blue arrow). This latter 'blue' mode was the only behavioral mode during which we observed in big brown bats a spectral peak at the theta frequency range (see ref. 4, their Fig. 4c-d). However, this latter behavioral mode is completely absent in the Egyptian fruit bat (panel b here), possibly because Egyptian fruit bats cannot reach very high sonar call-rates[11]. This behavioral difference between the two bat species might account for the absence in the Egyptian fruit bat of any spectral peak at the theta frequency range, in all behavioral combinations. **(e-f)** Theta-bouts do not modulate the bat velocity (**e**) or echolocation call-rate (**f**). Blue dots represent the mean velocity (**e**) and echolocation call-rate (**f**) during theta-bouts. Orange- and green-colored areas show the 95% confidence intervals for the velocity and echolocation call-rates, respectively. These confidence intervals were generated for each individual recording day by choosing random non-theta time epochs with total duration that matched the total time for all the theta-bouts observed on that day. The process was repeated 500 times for each day to generate the 95% confidence intervals. Only days for which more than 10 theta-bouts were detected were used for this analysis (14/17 days). Note that for nearly all days the data are not significantly different from chance.

Supplementary Figure 15 - Page 1

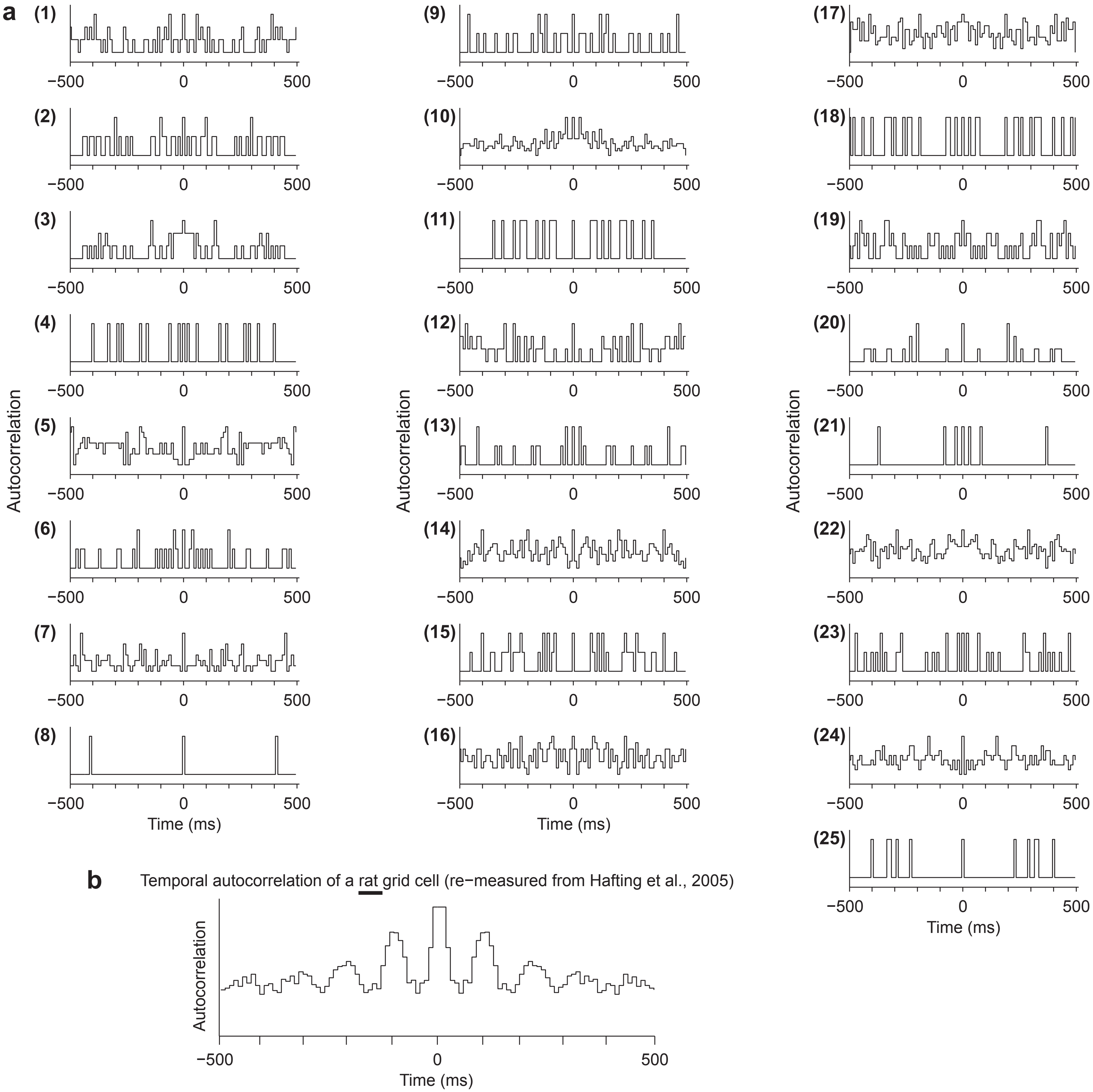

Supplementary Figure 15 - Page 2

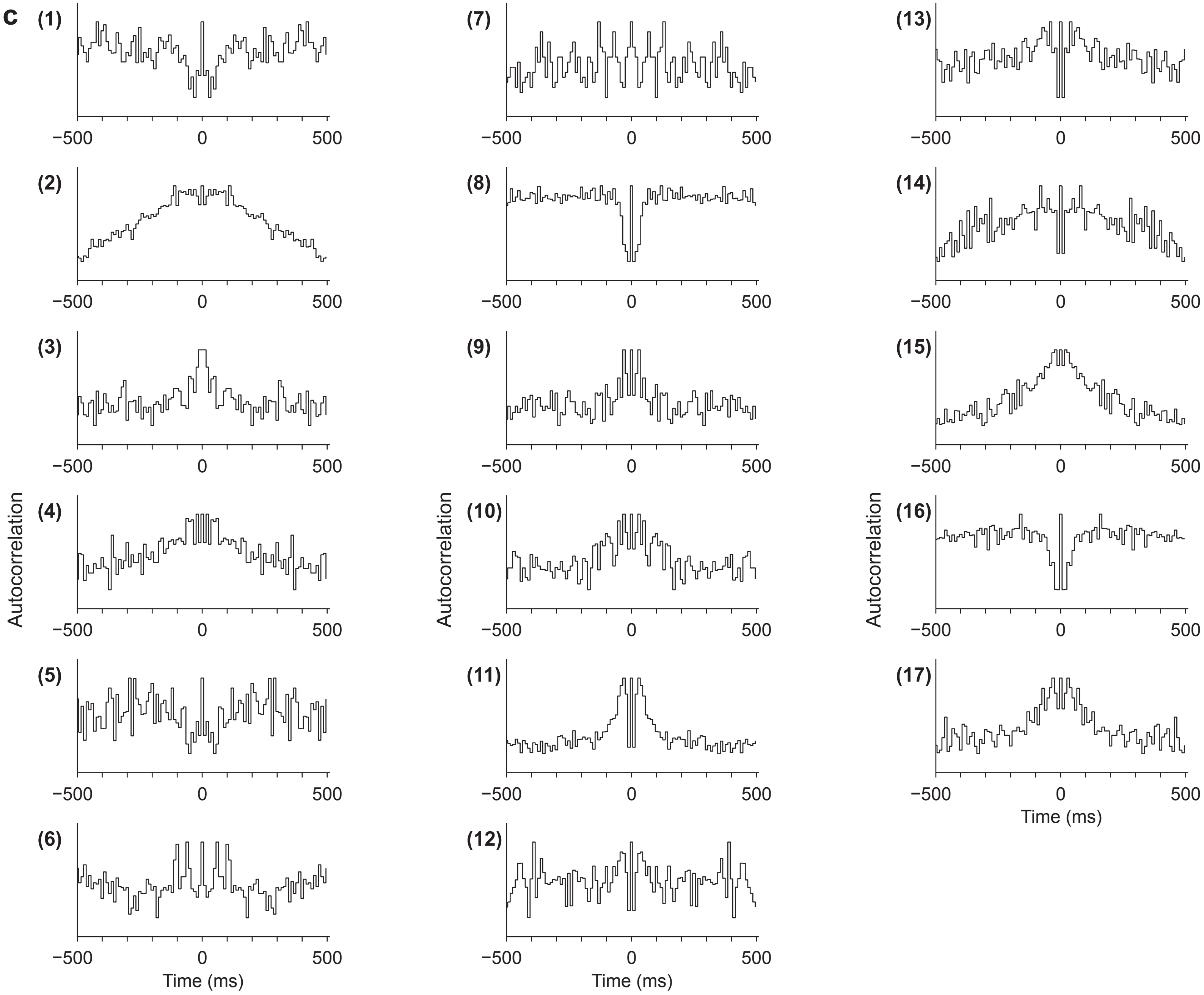

Supplementary Figure 15 | No theta modulated firing in the bat MEC. a, Spike-train autocorrelograms are shown for all grid cells. Grid cells are numbered in the same order as in figure 4i (left) of the main text. Note the absence of any clear temporal modulation in the theta range. Bin size, 10 ms. Notice that occasional peaks in individual bins of the autocorrelogram (such as in grid-cell # 24, for example) do not reflect a real theta rhythmicity in the spike train, as can be seen from the non-significant theta-index for the same cell in Fig. 4i of the main text. **b,** Spike-train autocorrelogram of a typical grid cell recorded in *rat* MEC (adapted from Hafting et al., 2005 (ref. 17), their Supplementary Fig. S1a; bin size,10 ms). Note the strong temporal periodicity of the spiking in the rat, at the theta frequency (~10-Hz frequency, 100-ms period) – very different from the lack of theta periodicity in the firing of bat grid-cells. **c,** Spike-train autocorrelograms for the multi-unit activity recorded in all sites (n=17) where grid cells were recorded. Sites are numbered in the same order as in Fig. 4h (right) of the main text.

Supplementary Figure 16

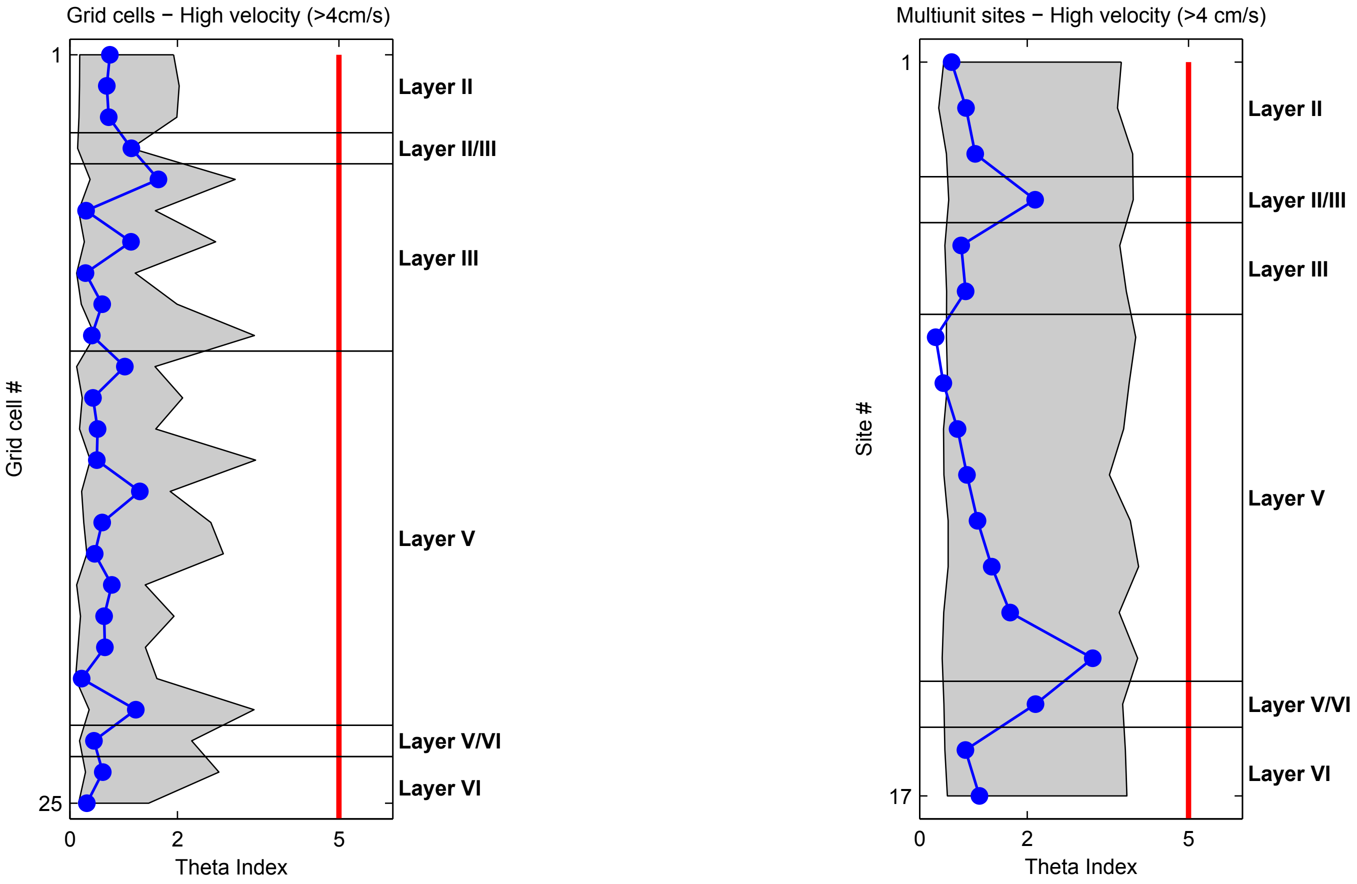

Supplementary Figure 16 | No theta modulated firing in bat MEC during high velocities. Theta index (see Supplementary Methods) for all the grid cells (left) and all the multi-unit sites where grid cells were recorded (right), computed for high velocities only (>4 cm/s). Cells ordered by the MEC layer in which they were recorded. Same notations as in Fig. 4h of the main text. Shaded area shows the 95% confidence interval (see Supplementary Methods). Red line denotes the theta-index threshold of 5, commonly used in rats[13]. Note that *none* of the theta index values obtained from single-unit grid cells, or from multi-unit activity recorded in sites where grid cells were recorded, ever exceeded the 95% confidence interval.

Supplementary Figure 17

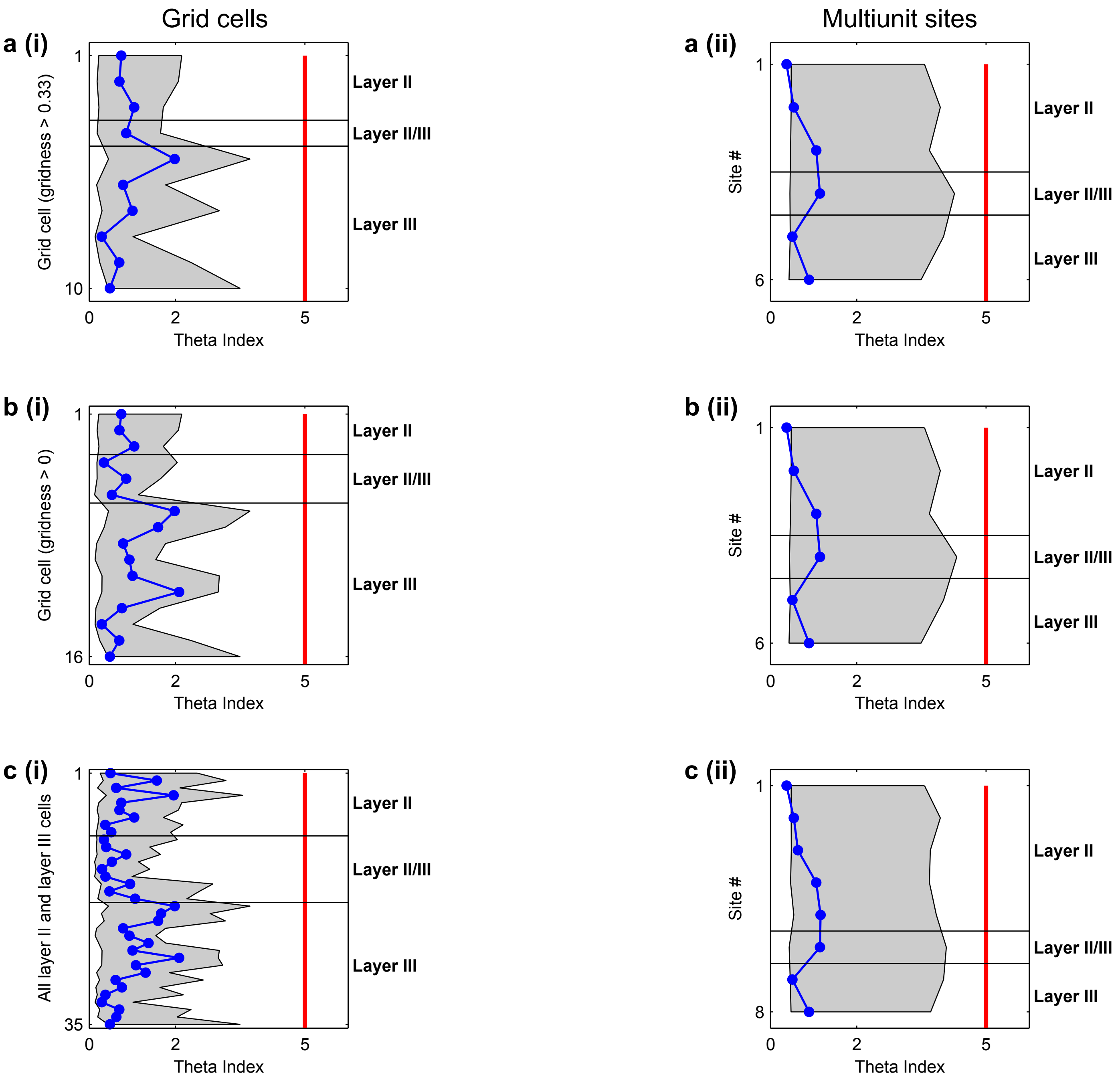

Supplementary Figure 17 | No theta modulated firing in the superficial layers of the bat MEC. Theta index (Supplementary Methods) for all the cells (left) and multi-unit sites (right), ordered by the MEC layer in which the cells were recorded. Same notations as in Fig. 4h of the main text. Data are shown for three cases: (**a**) Grid cell with a gridness score > 0.33 (the threshold set via random shuffling of the data – see Supplementary Methods). (**b**) Grid cells with gridness score > 0 (threshold previously used in several grid-cell studies in rats[18,35,37,38,39]). (**c**) All single units recorded from layers II and III of the bat MEC (n = 35 cells). Shaded area shows the 95% confidence interval (see Supplementary Methods). Red line denotes the theta-index threshold = 5, commonly used in rats[13]. Grid cells were recorded in 6 of the 8 recording sites in layers II and III. The anatomical locations of these 6 sites (as well as the locations of all the deep-layer recording sites) are shown in Supplementary Fig. 9. Note that *none* of the single units (whether grid cells or not) that we recorded in layers II and III of bat MEC – and *none* of the multi-units, in any of recording sites in layers II and III – ever showed a significant theta index.

Supplementary Figure 18

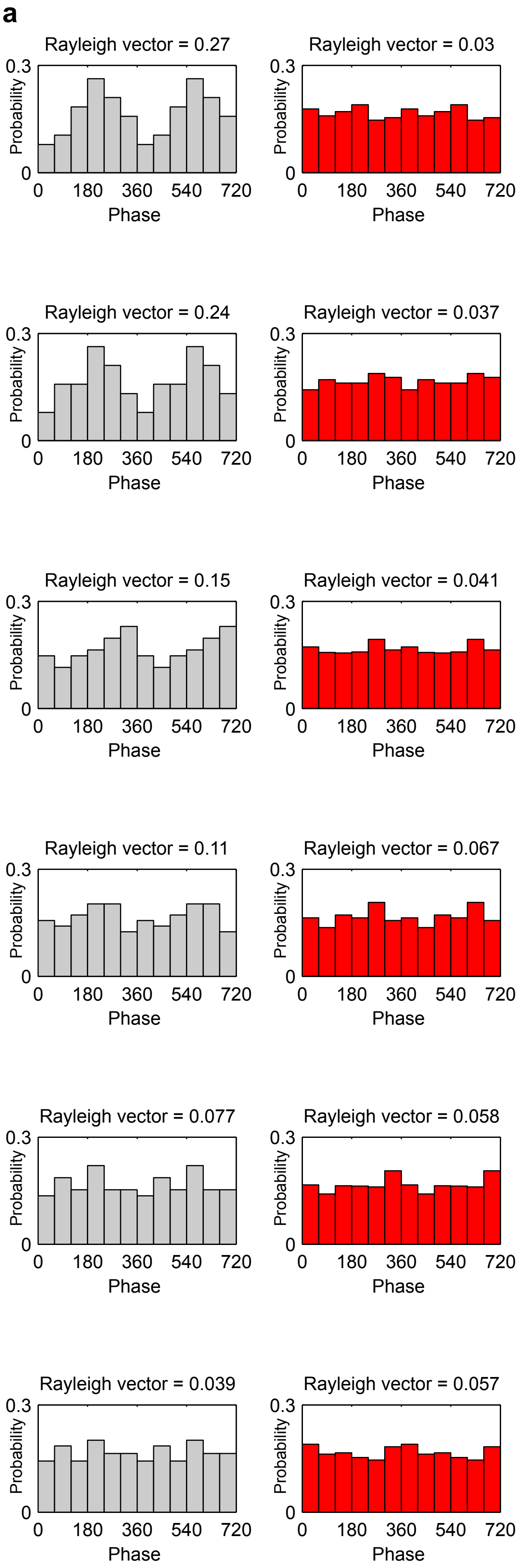

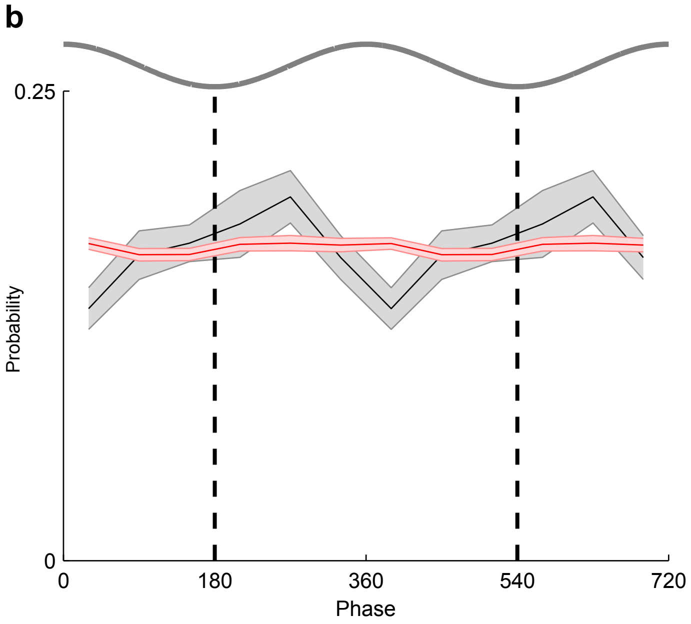

Supplementary Figure 18 | Neuronal firing in MEC is theta-modulated during theta bouts but not outside the theta-bouts.
a, Examples of phase distribution of six representative MEC neurons during theta-bouts (left, gray histograms) and during all other non-theta times (right, red histograms). The six examples are ordered by descending values of the Rayleigh vector of the gray distribution (top to bottom). Rayleigh vector values for each cell are indicated above the histograms.
b, Population average discharge probability of MEC neurons (same graph as Fig. 4i), showing clear theta-modulation during theta bouts (gray curve) but lack of theta-modulation during non-theta epochs (red curve). Both curves show mean ± s.e.m. In all plots, two theta cycles are shown for visualization purposes. Data from behavioral and sleep sessions were pooled together. Bin size, 60^{o}. Note the lack of theta modulation during non-theta times, in all the individual examples (panel a) and in the population average (panel b). During theta-bouts, the most common preferred phase of the theta-locked spikes occurred slightly after the trough of the locally-recorded theta wave (panel b, gray), similar to what is commonly observed in the rat[23,36].

Supplementary Figure 19

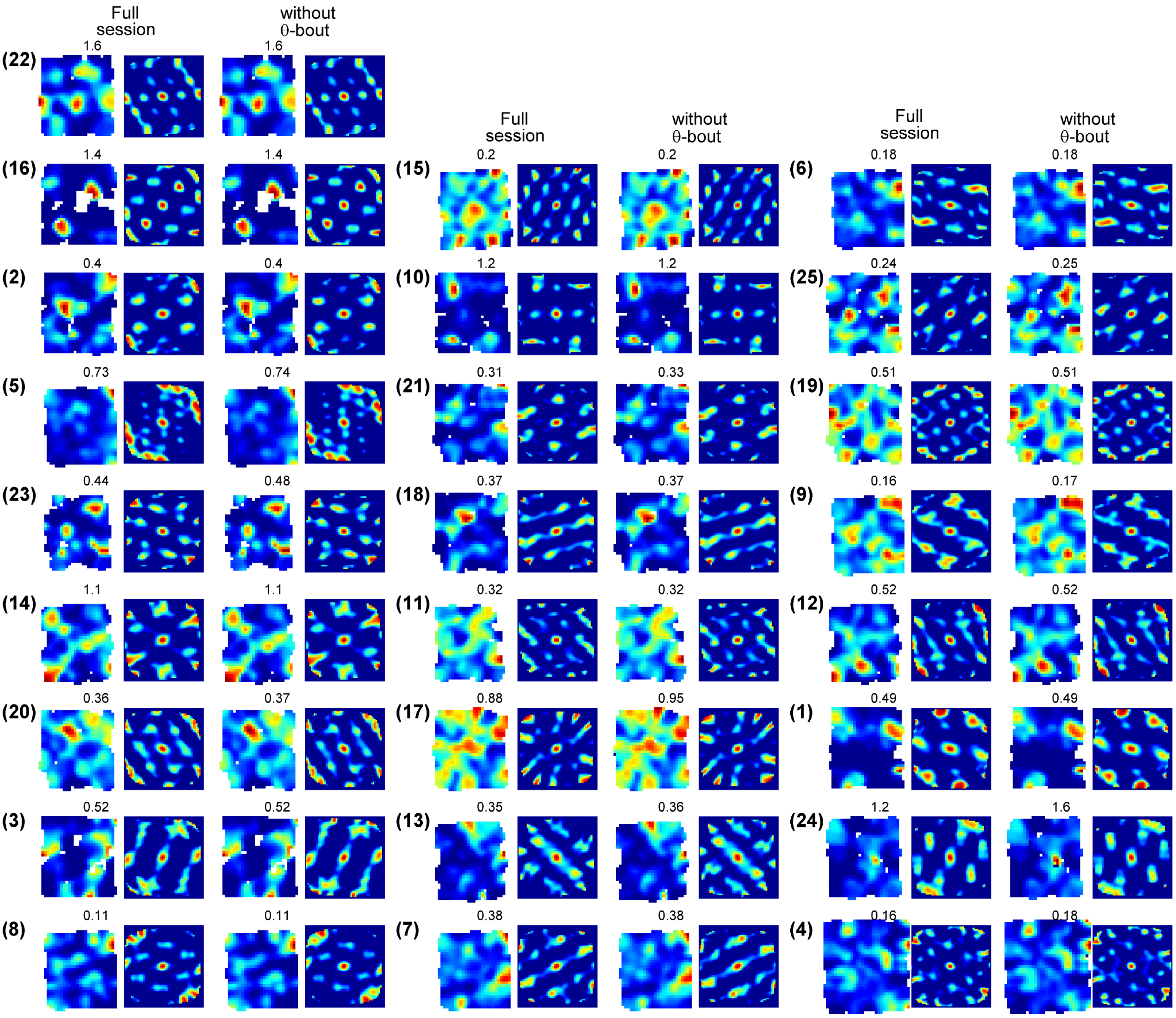

Supplementary Figure 19 | Removal of theta-bouts did not affect gridness. Rate maps and spatial autocorrelograms before (left pairs) and after (right pairs) the removal of theta-bouts (see Supplementary Methods): Shown here are the data for all grid cells (n=25). Cells are sorted by initial gridness value (descending order from top-left to bottom-right neuron). Numbers on the left of each cell correspond to the cell numbers in Fig. 4h and Supplementary Fig. 15a. Color scale of the rate maps is normalized to the maximal firing rate obtained from both maps for each neuron. Peak firing rate is indicated for each rate-map.

Supplementary Figure 20

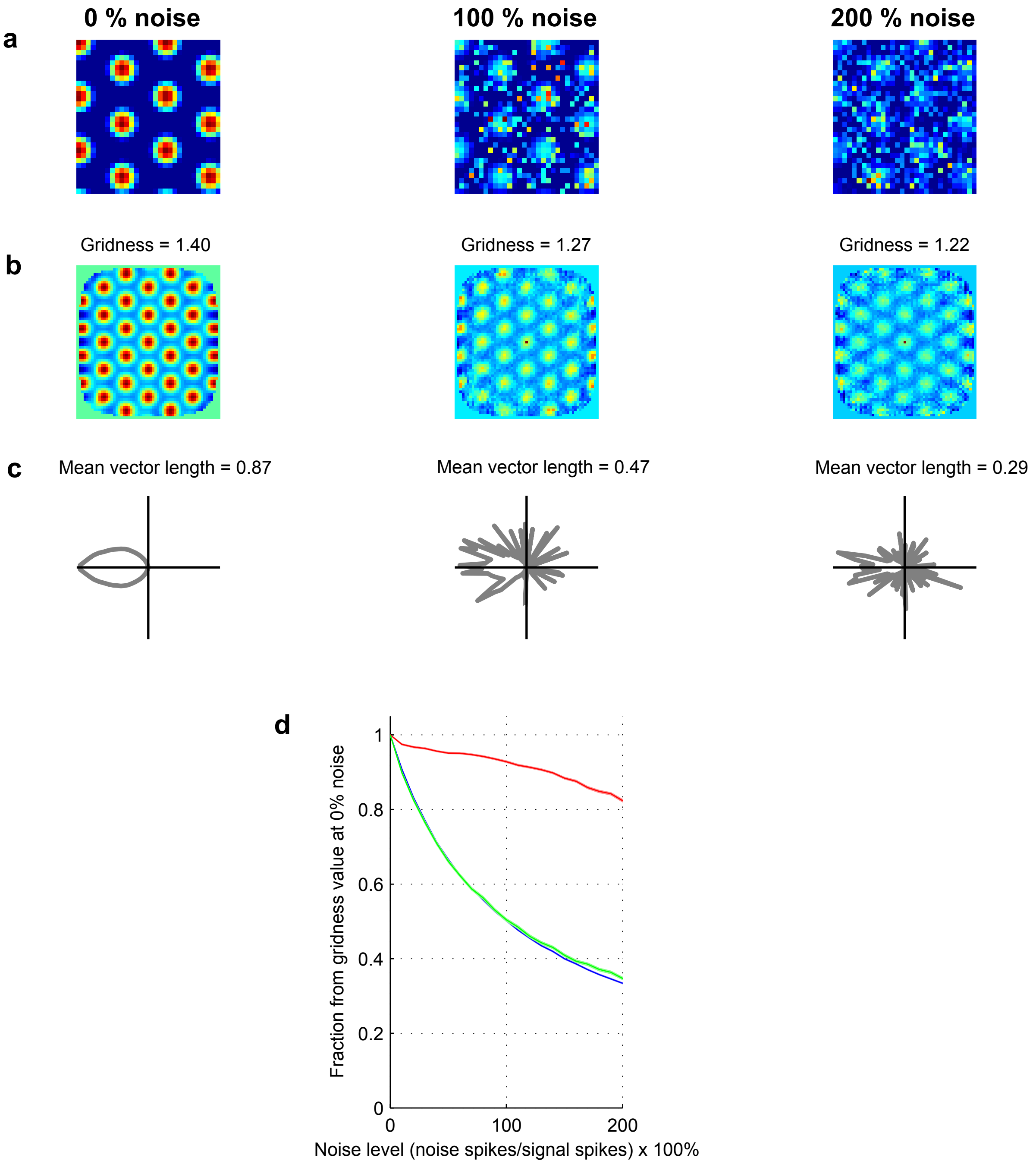

Supplementary Figure 20 | Effect of increasing the levels of spontaneous spiking on the values of spatial indexes: gridness and mean vector length indexes. We conducted here a robustness analysis, examining the effect of increasing the levels of spontaneous spiking (“noise levels”) on the gridness index and on the mean vector length index, by using simulations. First, an 'ideal' rate-map with perfect hexagonal grid was constructed, by combining three sinusoids at 60° to each other (**a** – left); its spatial autocorrelogram was computed (**b** – left); and its gridness index was then derived, as described in the Supplementary Methods. Subsequently, randomly distributed spikes ('noise spikes', uniformly distributed in the arena) were gradually added to the original rate map (**a** – middle and right panels); the autocorrelogram of these noisy rate-maps was then computed (**b** – middle and right), and their gridness values were derived.

Continued from previous page

The relative number of added "noise spikes" defined the percent of noise: We examined noise levels ranging from 0% noise (no added spikes) to 200% noise (the amount of "noise-spikes" equaled twice the amount of spikes in the original map), in steps of 10%. For each noise level, 500 permutations of randomly added noise spikes were analyzed. As expected, increasing levels of noise resulted in gradually decreasing gridness values (**d** – red curve, mean ± s.e.m). To assess the effect of noise levels on the mean vector length index – and to compare it quantitatively to the effects of noise on the gridness index – the two-dimensional vector comprising the grid rate-map was linearly transformed to a one-dimensional vector, while maintaining both the number of bins and the number of spikes, in order to avoid biases due to unequal bin number or unequal spike-counts. The linearized vector was then re-ordered (sorted) so that its highest value was placed in the center of the vector, and lower values alternated to the left and right of the peak – which created a nearly symmetric polar tuning curve (**c** – left); this curve, by construction, had the same number of bins and the same number of spikes as the corresponding grid rate-map (**a** – left); we then computed its mean vector length as described in the Supplementary Methods. Increasing the noise levels resulted in a rapid decline in the mean vector length index (**d** – blue curve, mean ± s.e.m) – a decline which was much steeper than that observed for the gridness index (compare to **d**, red curve). When we binned the polar map with a larger bin-size, similar to that used for real data in this work (3.6^o), and applied a smoothing procedure as described in the Supplementary Methods for real head-direction curves, no substantial change was found in the curve describing the effect of noise on the mean vector length index (**d** – green curve, mean ± s.e.m): The decline of the mean vector length index was still steeper than that observed for the gridness index. Thus, the results of this robustness analysis suggest that the gridness index is more robust to noise (spontaneous) spikes than is the mean vector length index; this robustness of the gridness index to noise is likely due to the additional processing (autocorrelation of the rate map) which is used to derive the gridness index, and which effectively smoothes out the noisy spikes.

Importantly for our data, this differential effect of spontaneous noise spikes on these two indexes might account for the relatively low proportion of neurons with significant head-directional tuning that we observed in our recordings in Egyptian fruit bat MEC (Fig. 3g): The relatively low firing-rate in the bat (compared to the rat) results in lower signal-to-noise levels in the bat, and under these circumstances, the mean vector length index is much more degraded than the gridness index. Thus, while the proportion of grid cells in our bat-MEC data is similar to those reported in the rat[13,18], we detected a smaller proportion of head-direction cells in bat MEC compared to rat MEC when using the (noise-susceptible) mean vector length index.

Supplementary Figure 21

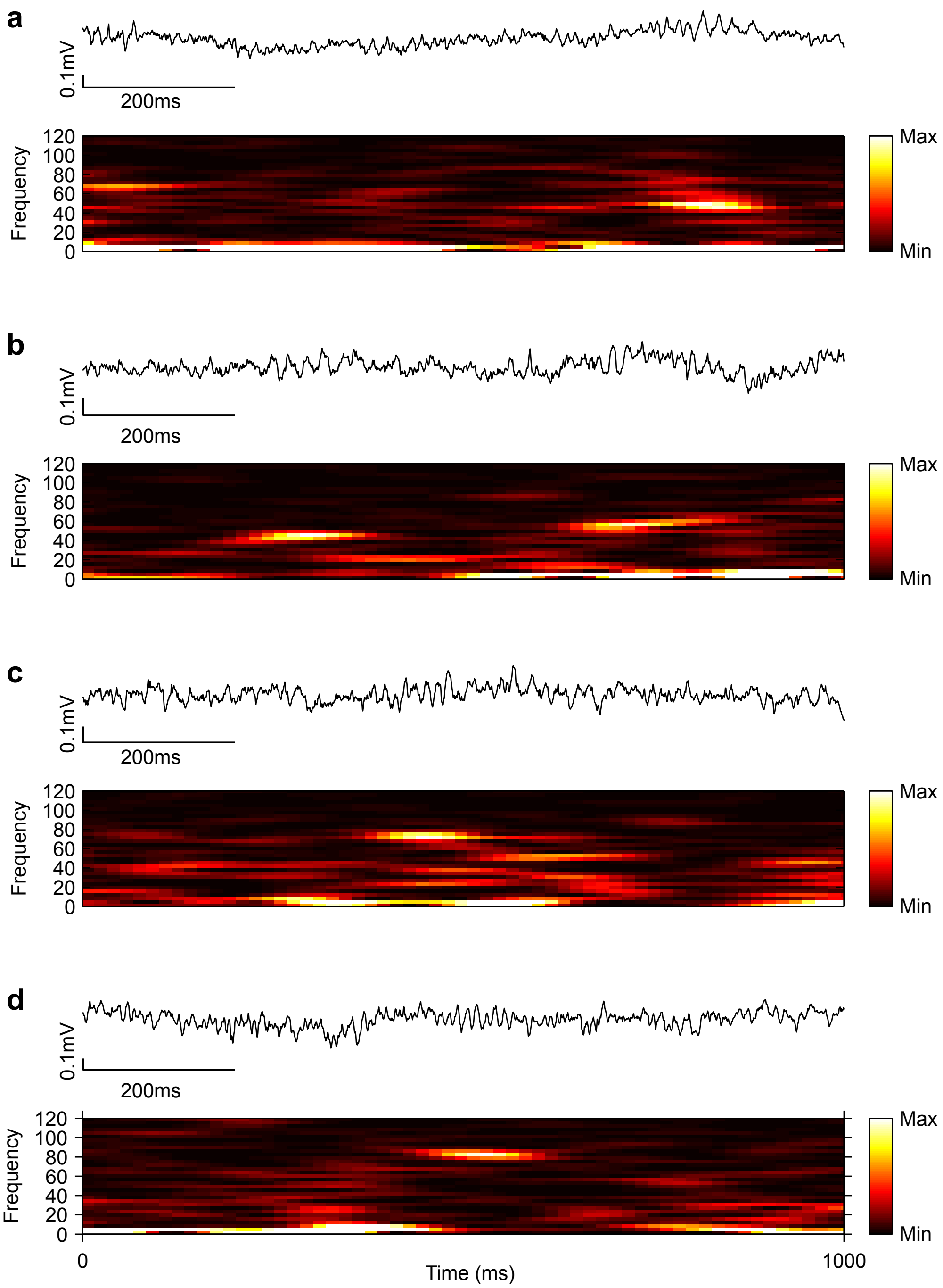

Supplementary Figure 21 | Examples of Gamma oscillations in the bat MEC. (**a-d**) Four examples of 1-s raw LFP traces (top traces, unfiltered 1-475 Hz) and corresponding spectrograms (bottom, frequency x time representation), showing gamma bouts recorded during behavior sessions in 2 different days from two bats. Note that, similar to the rat[24,25], gamma in the bat MEC appeared over a broad range of frequencies, from slow gamma (~25-50 Hz) to fast gamma (~65-140 Hz).

Supplementary Figure 22 - Page 1

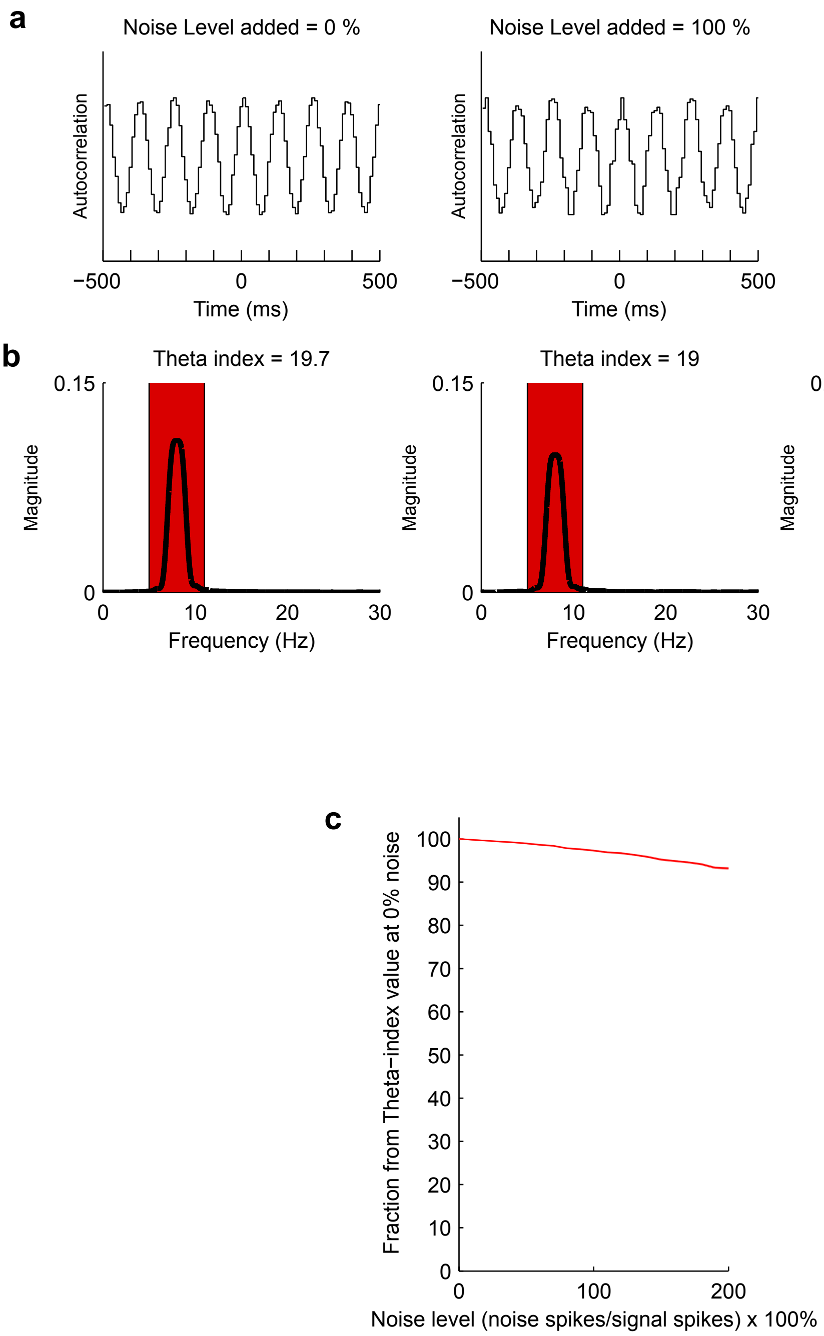

Supplementary Figure 22 | Effect of increasing the levels of spontaneous spiking on temporal measures: theta index. We conducted here a robustness analysis, examining the effect of increasing the levels of spontaneous spiking (“noise levels”) on the theta-index, using simulations. First, an 'ideal' theta-modulated spike train (**a** – left) was constructed by simulating a simple Poisson spiking neuron with a sinusoidally-modulated spiking probability. Subsequently, we added randomly-distributed spikes ('noise spikes', uniformly distributed in the behavioral recording session, which was defined for the purpose of this simulation as lasting 20 minutes); these noise spikes were gradually added to the original spike train, and the temporal autocorrelograms of the noisy spike-trains were then re-computed (**a** – middle and right), and their theta-index values were derived in the same way as explained in the Supplementary Methods (**b**).

Continued from previous page

We examined noise levels ranging from 0% noise (no added spikes) to 200% noise (the amount of “noise-spikes" equaled twice the amount of spikes in the original sinusoidally-modulated spike train); noise levels were increased in steps of 10%. For each noise level, we generated 500 permutations of randomly added noise spikes (**c** – red curve, mean ± s.e.m. over these 500 permutations). As expected, increasing levels of noise resulted in gradually decreasing theta-index values; however, even under the highest noise levels that we examined, theta modulation was still clearly observed in the autocorrelograms (panels **a-b**, right), and it was well detected via the theta-index measure – as indicated by the small decrease from baseline (less than 10% decrease: panel **c**, red curve). This analysis shows that the theta-index measure is robust even under conditions when the ratio between the number of 'signal spikes' and spontaneous spikes is relatively low, as is the case in low-firing-rate neurons. The results of this analysis suggest that theta modulation, if present, should be detected even in low-firing-rate neurons, via the theta-index measure that was used in this study.

Supplementary Methods

Subjects

Neural activity was recorded from 5 adult male Egyptian fruit bats, *Rousettus aegyptiacus* (weight 152–172 gr at implantation): 3 bats were used for recordings from the medial entorhinal cortex (MEC), and 2 bats for recordings from dorsal hippocampal area CA1 (see below). This bat species belongs to the sub-order Megachiroptera (Pteropodidae), or megabats[1-3], and are ~10 times larger in size than the big brown bat whose hippocampus we studied previously[4,5] (weight 14–18 gr). The larger size of Egyptian fruit bats was important in this experiment for several reasons: (i) They could carry the recording device on their heads much more easily during free behavior; (ii) The larger size of their brain[6] assisted in precise identification of recording locations and layers in the entorhinal cortex; (iii) Their size allowed for good behavioral coverage of the large arena used in this study (117 × 117 cm, see below). Bats were collected from the wild and housed in a large communal flight room (6 × 6 m) at the bat breeding colony of the Weizmann Institute of Science, for an acclimation period of at least 1-month prior to initiation of behavioral training. Throughout this period, and then during behavioral training and electrophysiological recordings, the bats were kept on a 12-hr reversed light-dark cycle. All training and testing procedures were conducted during the dark cycle. Subsequently, bats were moved to laboratory facilities where they were housed in cages (2–5 bats per cage) and maintained in a humidity- and temperature-controlled room. In addition, 8 adult naïve bats were perfused and their brains were used for immuno-histochemical staining to delineate the anatomy of the hippocampal formation, and in particular the borders of MEC and its detailed laminar structure (Fig. 2a and Supplementary Figs 5–6; see below). Experimental procedures were approved by the Institutional Animal Care and Use Committee of the Weizmann Institute of Science.

Behavioral setup and training

Behavioral arena

The training and recording arena used throughout this study was a 117 × 117 cm square arena (Fig. 1b); the same arena was used for MEC and CA1 recordings. The arena had 70-cm high walls, its floor and walls were colored in black, and a portion of one of the walls was painted white and served as a polarizing cue (42 width × 70 cm high white cue card; see Fig. 1b, white stripe). The arena was placed horizontally on the floor of a large room; the position of the arena within the room was nearly fixed throughout the duration of training and testing, and the locations of its four corners were calibrated daily during the testing period (see below).

On two recording days in MEC, a larger novel arena (160 × 160 × 70 cm) was tested, but was not used anymore because it was difficult for the bat to cover well this large area by crawling; during these two days, 14 neurons were recorded (including one grid cell).

Training

Bats were trained to crawl freely on the floor of the arena while searching for small pieces of fruit randomly scattered inside the arena. This "food chasing" task is commonly used in studies of the hippocampus and entorhinal cortex, as it facilitates good behavioral coverage of a two-dimensional environment by the animal[4,7,8]. Training lasted between 1.5 and 6 months per bat (typically 3-4 months) prior to surgery; the long training duration was due to the need to train bats to crawl quickly for long periods of time (in order to obtain good behavioral coverage of the arena) while avoiding their natural instinct to fly out of the arena. Training progressed in several stages: First, bats were trained not to fly out of the arena (by physically blocking them from above), while eating fruit pieces given to them on the arena floor. Next, bats were trained to crawl within the arena and collect individual pieces of fruit, until the amount of fruit dedicated to the training session was consumed (usually ~ 25–40 gr of fruit). At these early stages, rapid crawling was still not a requirement, and the duration of the training session was not limited in time and could last several hours. As training progressed, over the course of several months, the number of available pieces of fruit inside the arena at any given moment was reduced, and the duration of individual training sessions was also gradually reduced, thus forcing the bats to traverse increasingly larger distances between one piece of fruit and the next one, at progressively shorter times. Bats were not allowed to fly within the arena to get from one piece of fruit to the next, and were only allowed to move within the arena by crawling. Towards the final stages of training, and then during the electrophysiological recordings, only banana was used as food reward inside the arena, because: (i) these fruit bats have strong preference for banana, and (ii) the softness of the banana requires minimal application of biting force by the jaw muscles of the bats during chewing, which resulted in very small chewing artifacts during electrophysiological recordings, and often no artifacts at all – thus facilitating high-quality recordings. The bats received also daily supplements of less-preferred fruits (such as apples) in their home cage, in order to maintain their body weight within 85% of their *ad libitum* weight.

All training and testing were done under low-light conditions (illuminance 1–2 lux; measured using ILT-1700 illuminance meter, International Light, MA) – a light level that was low enough not to stress them, but which provided enough light for these highly-visual bats[2,3,9] to clearly see the environment and to use visual cues.

Experimental design

At the start and end of each recording day, the arena floor was thoroughly cleaned with water and with 70% ethanol, to remove odors. Two sleep sessions flanked the behavioral session: sleep → behavior → sleep. During behavior, the bat was required to crawl continuously within the arena to obtain food reward. The duration of the behavioral session was variable and often continued until proper coverage of the arena was obtained; this duration varied between 20–60 minutes. The durations of the sleep sessions were less variable and usually lasted 15 minutes. During the sleep sessions, the bat was comfortably placed inside a holding bag, with its head and neck outside the bag, and rested on a pedestal next to the behavioral arena, facing away from the arena.

Video and audio recordings

The position of the bat's head was recorded using a video tracker (Neuralynx), which tracked the positions of two light-emitting diodes located at the top of the preamplifier, and these positional data were stored with a 25-Hz sampling rate. The bat's location was taken as the center-point between the two diodes; additionally, because the diodes were of different colors (red and blue), we could compute the bat’s head direction (see below).

The location of the behavioral arena relative to the camera was nearly fixed, but nevertheless we calibrated it daily. At the beginning of each day, the experimenter verified that the full extent of the behavioral arena was fully covered by the camera's field of view. Upon the completion of the daily recordings, the location of the arena was calibrated in the coordinate-frame of the video tracker, by recording the locations of battery-operated light-emitting diodes placed at the four corners of the square arena.

The timing of the bat's echolocation calls was recorded by filtering a 31–39 kHz frequency slab, and heterodyning it down in frequency to 0–8 kHz using a bat detector (D-230, Pettersson Elektronik) and then sampling it continuously at 16 kHz (Cheetah data acquisition system, Neuralynx). The heterodyning distorted the detailed structure of the echolocation calls, but permitted an accurate measurement of call timing (Supplementary Fig. 14). Echolocation calls in this bat species occur in characteristic double-clicks with 20-ms intervals[10,11] (see example in Supplementary Fig. 14a); these clicks were detected offline via a threshold-crossing algorithm. Clicks with intervals under 30-ms were merged, to avoid contamination by returning echoes that may cross the detection threshold: This resulted in each double-click being counted as one call; hence, the call-rates shown in Supplementary Fig. 14b and 14f refer to the rates of merged double-clicks.

Calibration of auditory recording quality was conducted daily both before and after the neural recordings. Specifically, a sequence of clicks was produced by a dog-clicker, a device which produces clicks of fixed amplitude, and this calibration sequence of sounds was recorded (Neuralynx Cheetah) and stored together with the neural and behavioral data recorded on that day.

Surgery

Upon completion of the behavioral training, the bats underwent surgery to implant a tetrode microdrive. Anesthesia was induced either by use of isoflurane (placing the bat in an induction chamber at 5% isoflurane for ~2 minutes; 3 bats), or by an injectible anesthesia cocktail of ketamine 15 mg/kgBW and medetomidine 0.06 mg/kgBW (2 bats). Subsequently, the bat was placed in a stereotaxic apparatus (Kopf) and anesthesia was maintained throughout surgery by isoflurane in 98% oxygen (usually levels of 1–2% isoflurane were sufficient to maintain anesthesia, but sometimes higher levels were used). The depth of anesthesia was monitored by testing toe pinch reflexes and constantly monitoring the bat's breathing rate. The body temperature of the bat was kept constant at approximately 36°C, using a closed-loop temperature controller (FHC) connected to a rectal temperature probe and a heating-pad placed under the bat.

Bats were implanted with a four-tetrode lightweight microdrive (4-drive, Neuralynx; weight 2.1 gr). Tetrodes (~ 45 µm diameter) were constructed from four strands of platinum-iridium wire (17.8 µm diameter, HM-L insulated), bound together by twisting and then melting their insulations. Each of the four tetrodes was loaded and glued separately into a telescoped assembly of polyimide tubes mounted into the microdrive. The tetrodes exited the microdrive through a guide cannula in an approximately rectangular arrangement with 300–600 µm horizontal spacing between tetrodes. Each tetrode could be moved independently via a separate drive screw (160 µm per turn), thus allowing accurate placement of each tetrode at the desired depth. On the day before surgery, the tip of each tetrode was cut flat using high-quality scissors (tungsten-carbide scissors with ceramic coating; FST, CeramaCut) and gold-plated to reduce the impedance of individual wires to 0.3–0.8 MΩ (at 1 kHz).

While the bat was under isoflurane anesthesia, the skull was micro-scarred to improve subsequent adhesion, and a circular opening (craniotomy of 1.8-mm and 2.2-mm diameter for hippocampal and MEC implants, respectively) was made in the skull over the right hemisphere. The coordinates of the craniotomy depended on the targeted brain region, dorsal hippocampal CA1 (2 bats) or MEC (3 bats). For dorsal CA1, the center of craniotomy was 8.5 mm anterior to the earbars and 3.1 mm lateral to the midline (N. Ulanovsky and R. Eilam, Stereotaxic brain atlas of the Egyptian fruit bat, in preparation). For implants targeting the MEC, the center of craniotomy was 4.5 mm lateral to the midline and 0.7 mm anterior to the transverse sinus that runs between the posterior part of the cortex and the cerebellum. After removal of the dura, the microdrive was lowered and the tip of the microdrive's guide tube was placed on the brain surface. The angle of placement depended on the targeted brain region: For dorsal CA1 implants the microdrive was placed vertically. For MEC implants, the microdrive was angled 38^o horizontally and 24^o vertically – these angles are in the spherical coordinates of the stereotaxic apparatus, which translates to angles of 15^o anteriorally in the sagittal plane and 19^o laterally in the coronal plane. The angling laterally was required because the MEC in bats is located more laterally than the MEC in rats; we targeted MEC areas located > 6-mm lateral to midline. These angles allowed the tetrodes to move almost parallel to the cortical layers in MEC recordings, and perpendicular to the CA1 pyramidal layer in CA1 recordings. For MEC recordings, the tip of the microdrive guide-tube was cut at an angle of 24° (matching the net vertical tilt of the microdrive), to allow nearly horizontal placement of the tip of the guide tube onto the brain surface. The craniotomy was then filled with a biocompatible elastomer (Kwik-Sil, World Precision Instruments) to protect the brain. The exposed muscle tissue was then covered with a thin layer of biocompatible adhesive (Vetbond, World Precision Instruments) for protection. A bone screw (FST) with a soldered stainless-steel wire was fixed to the skull in the frontal plate, and served as a ground screw after its electrical connection to the dura was verified. An additional set of 3–5 bone screws were fixed to the skull and served as anchor screws for mechanical stability of the implant. The bases of the screws were then covered with a thin layer of medical-grade cyanoacrylate adhesive (Loctite 4161) which held the screws firmly to the skull; and then dental acrylic was added to secure the entire microdrive to the screws and to the skull.

Electrophysiological recordings

During a period of ~1 week after surgery, the tetrodes were slowly lowered towards either the CA1 pyramidal layer or towards MEC. In all cases, one of the tetrodes served as a reference electrode and was left in an electrically-quite zone; we periodically verified the quietness of the reference tetrode by examining its activity against the ground screw. For CA1 recordings, the reference tetrode was left in an electrically-quite zone in the white matter above the CA1 pyramidal cell layer (except the last 2 recording days in one of the bats, where we used a reference placed below the CA1 pyramidal layer in an electrically quite area). For MEC recordings, the reference tetrode was left in the cortex, dorsally to the postrhinal/MEC border – well away from the recording locations in MEC (see example in Supplementary Fig. 7 – "yellow" tetrode). This reference tetrode was used for differential (double-ended) recordings. The remaining three tetrodes in each bat served as recording tetrodes, although for 4 of the 5 bats we were able to obtain high-quality recordings from only one recording tetrode per bat (for one MEC bat, two tetrodes were successfully placed inside MEC; see Supplementary Fig. 8d and Supplementary Fig. 7, red and green dots).

For CA1 recordings, the position of tetrodes in the CA1 pyramidal cell layer was provisionally determined by the presence of high-frequency oscillations (ripples) in the local field potential (LFP), as detailed below, and was subsequently verified histologically.

For MEC recordings, the presence of high-frequency ripple oscillations was only used as a suggestive indication for the positioning of the tetrodes, because ripples in MEC are much more variable than ripples in CA1 (see main text). As an additional indication of tetrode location within MEC for each particular day, we spike-sorted (at the end of each recording day) the neurons recorded on that day, and their firing-rate maps were constructed (see below): The appearance of grid-like firing patterns was also used as an indication for the positioning of tetrodes in MEC. The precise positioning of each tetrode for each recording day was later reconstructed histologically (see below). Regardless of the quality of the recordings, tetrodes were never kept in the same position between days, and were always moved at the end of each recording day (40–200 μm daily), in order to obtain recordings from new ensembles of neurons daily.

During recording, a unity-gain preamplifier (HS-16 or HS-18, Neuralynx) was attached to a connector on top of the 4-tetrode microdrive via a light-weight tether which was also attached to a pulley to keep the tether straight at all times. Signals from each of the tetrode's four wires were amplified (1,400–5,000×) and band-pass filtered (600–6,000 Hz; Lynx-8, Neuralynx). A voltage threshold (30–50 μV) was used for collecting 1-ms spike waveforms, which were sampled at 30.3 kHz (0.25 ms before the peak of the spike and 0.75 ms after; Neuralynx Cheetah). Local field potentials (LFP) were recorded from all tetrodes ; specifically, one of the wires of each recording tetrode was also used for collecting continuous recordings of the local field potential from that tetrode (LFP: 1000× gain, 1–475 Hz filtering, 1.9-kHz sampling rate). When comparing LFP to spike recordings, we always used the LFP recorded on the same tetrode on which the spikes were recorded.

For dorsal CA1 hippocampal recordings, tetrodes were moved either upward or downward, to maximize the quality of the neural signal recorded on each day. For MEC recordings, the tetrodes were moved only in the downward direction (40–200 μm daily) and were never moved upward: Although this conservative approach reduced the amount of collected data, it allowed more accurate estimation of the daily recording locations in MEC during histological analysis, which permitted us in many cases to identify to precise cortical layer in which each neuron was recorded (see below). In one of the bats, where two tetrodes were successfully placed inside MEC, electrolytic lesions (DC positive current of 30 μA, 15-s duration) were done after the last day of recording (Fig. 2b, and Supplementary Fig. 7 - panel #8) to assist in the precise reconstruction of tetrode positions.

All types of data (spikes, LFP, video and audio) were time-stamped with the same 1-MHz clock (Digital I/O, Neuralynx). Data were collected continuously throughout all the behavioral and sleep sessions of each recording day (~1 – 1.5 hours daily).

Spike sorting

Spike waveforms that occurred simultaneously (within < 0.5-ms) on *all* the 3 recording tetrodes were treated as artifacts and discarded from subsequent analysis. The remaining waveforms were spike-sorted on the basis of their relative energies and amplitudes on different channels of each tetrode. A clustering software (SpikeSort3D, Neuralynx) was used to isolate clusters of single units. Each spike was graphically positioned in a two- or three-dimensional graph representing the energy or amplitude of the spike on two or three of the tetrode's four channels. Convex hull boundaries and template-matching of waveforms were used to identify well-separated clusters of spikes, which were individually color coded (Supplementary Fig. 1). Data from all three sessions (behavioral + two sleep sessions) were spike-sorted together. The well-separated clusters were further examined to ensure that they indeed represented the spikes of a single unit: First, we checked that a refractory period (2 ms) was present in the inter-spike interval histogram (Supplementary Fig. 2); second, that the amplitude of all the waveforms from each cluster were well above the voltage threshold of the data acquisition system (to ensure that the voltage threshold was not cutting a low-amplitude cluster in the middle). Finally, the quality of cluster separation was verified by computing the 'isolation distance' index[12], a standard index that calculates the distances between clustered spikes of different cells in Mahalanobis space using principal components and spike energy features[12]. Median isolation distances for CA1 neurons were 37.3 (22.1 – 52.2 interquartile range), and for MEC the median was 21.6 (13.0 – 30.1 interquartile range). These values are similar to those reported for rats[13,14].

For hippocampal CA1 recordings, complex-spike cells (excitatory, putative pyramidal neurons) were identified according to the following criteria: (i) The waveforms of each neuron had a characteristic shape with a narrow peak followed by a long after-hyperpolarization trough (Supplementary Figs 1a and 2a). (ii) The mean firing rate over all three sessions was < 5 Hz. (iii) Analysis of the neuron's inter-spike interval histogram revealed a tendency to fire in complex-spike bursts, as evidenced by the bimodal shape of the interval histogram, with a clear peak at short inter-spike intervals of 5–10 ms (Supplementary Fig. 2a, right).

For MEC recordings, we did not attempt to identify the neuronal class; instead, we took for analysis all the well-separated single units that passed the spike-sorting criteria (see above). Interestingly, unlike place-cells in CA1 that tended to be bursting (complex spike) cells – with many short inter-spike intervals of ~10 ms (Supplementary Fig. 2a, right) – most MEC grid cells tended to be non-bursting and did not show any peak at short inter-spike intervals (Supplementary Fig. 2b, right).

Overall, we recorded a total of 64 well-separated neurons from the dorsal hippocampal CA1 region of two bats (data recorded on two tetrodes in hippocampal CA1– one in each bat), and 74 well-separated neurons from MEC of three bats (data recorded on 4 tetrodes in MEC, one tetrode/bat in two bats and two tetrodes in the third bat). We excluded from further analysis neurons that fired less than 50 spikes during the behavioral session. A substantial portion of the CA1 neurons were active during the sleep sessions but not active during behavior (21/64 neurons were ‘behaviorally silent cells’: 33% of total cells); in contrast, in MEC very few neurons were silent during the behavioral session (4/74 cells). Thus, a total of 43 neurons from hippocampal area CA1 and 70 neurons from MEC were defined as ‘behaviorally active-cells’, and were included in the analyses below.

Data analysis

Firing-rate maps

The position of the animal’s head was computed as the center-point between two tracked LEDs (blue- and red-colored; see above); subsequently, the *x*- and *y*-coordinates of the position were each smoothed with a 15-point moving average filter. Firing-rate maps of single units were computed by partitioning the arena into either $4.6 \times 4.6\ \text{cm}^2$ bins (for MEC recordings) or $5.8 \times 5.8\ \text{cm}^2$ bins (for hippocampal CA1 recordings), and computing the time-spent in each bin and the spike-count per bin. These two maps (time-spent and spike-count) were then individually smoothed using a Gaussian kernel with standard deviation of $\sigma = 1.5$ bins. The firing-rate map was then computed for each neuron by dividing bin-by-bin the two smoothed maps of spike-count and time-spent. Unvisited bins (where total time-spent, before smoothing, was < 300 ms) were discarded from analysis and are shown as white bins on plots of firing-rate maps. The peak firing-rate was defined as the highest observed firing-rate in any of the bins of the firing-rate map.

Analysis of place cells

The spatial information, in bits per spike[4,15,16], was calculated for each cell as:

$$\text{spatial information (bits/spike)} = \sum p_i \, (r_i / r) \log_2(r_i / r)$$

where r_i is the firing rate of the cell in the i-th bin of the place-field, p_i is the probability of the animal being in the i-th bin (time spent in i-th bin / total session time), $r = \sum p_i r_i$ is the overall mean firing rate, and i is running over all the bins where the bat spent ≥ 300-ms. Place cells were defined as neurons with spatial information > 0.5 bits/spike.

Analysis of grid cells

To examine the periodic structure of the multiple firing fields of individual cells in the bat MEC, we calculated the two-dimensional spatial autocorrelation of the firing-rate map of each cell[17,18]. The spatial autocorrelogram of the firing rate map was calculated as:

$$r(\tau_x, \tau_y) = \frac{n\sum \lambda(x,y)\lambda(x-\tau_x, y-\tau_y) - \sum \lambda(x,y) \sum \lambda(x-\tau_x, y-\tau_y)}{\sqrt{n\sum \lambda(x,y)^2 - (\sum \lambda(x,y))^2}\sqrt{n\sum \lambda(x-\tau_x, y-\tau_y)^2 - (\sum \lambda(x-\tau_x, y-\tau_y))^2}}$$

Where $\lambda(x,y)$ denotes the average rate of the neuron at location (x,y), and τ_x and τ_y denote the spatial lags between the original and shifted firing rate maps. The summation was done over all n bins in $\lambda(x,y)$ for which the rate was estimated both for $\lambda(x,y)$ and $\lambda(x-\tau_x, y-\tau_y)$ (i.e., for which the bat spent > 300-ms inside the bin). No smoothing was applied to the autocorrelogram. Bins in the autocorrelogram were not computed (and left blank) for shifts x,y for which the total number of overlapping bins between the original and shifted maps was < 30. The spatial scale in the autocorrelogram is double that in the original rate-map (compare Fig. 2g and 2f).

To assess the degree of hexagonal 60° spatial periodicity for each neuron, we computed a commonly-used 'gridness index', and determined its statistical significance[13,14,18,19]. First, an annulus was extracted from the spatial autocorrelogram, as follows (Supplementary Fig. 10d): The outer radius of the annulus was taken as the distance to the furthest of the six peaks closest to the center of the autocorrelogram, multiplied by 1.15 ; the inner radius of the annulus was used to exclude the central peak of the autocorrelogram, and it was taken as the distance from the center where the correlation value dropped below 0.1 (Supplementary Fig. 10d). The annulus was then rotated in steps of 6^o and the Pearson correlation coefficient was computed between each of the rotated maps and the original map. For grid cells, the correlation values varied in a sinusoidal manner as a function of rotation, as expected from a hexagonal structure composed of equilateral triangles (Supplementary Fig. 10e). The gridness index was defined as the difference between the minimal correlation value at 60^o and 120^o (Supplementary Fig. 10e, red lines) and the maximal correlation value at 30^o, 90^o and 150^o (blue lines):

$$gridness = \min(r \text{ at } 60^\circ, r \text{ at } 120^\circ) - \max(r \text{ at } 30^\circ, r \text{ at } 90^\circ, r \text{ at } 150^\circ)$$

A shuffling procedure was applied to determine the significance of each neuron's gridness value[13,14,19]. For each recorded MEC neuron, the entire sequence of spikes was shifted in time by a random (uniformly-distributed) interval between 20 seconds and the duration of the session minus 20 seconds; the end of the session was wrapped to the beginning. This preserved the spike number and the temporal structure of the neuron's firing pattern, but dissociated the time of spiking from the animal's original trajectory. This procedure was repeated 100 times for each neuron (7,000 times for the 70 behaviorally-active neurons recorded in MEC). For each repetition, the firing rate and autocorrelation maps were computed in the same manner as described above, and the gridness index was computed. The 95th percentile of the resulting overall distribution of shuffled gridness values was then defined as the gridness threshold (Fig. 2h, red line). Cells with gridness index exceeding this threshold were defined as grid cells (Fig. 2i). A total of 25 grid cells passed this criterion. The distribution of gridness scores, for both the recorded and shuffled data, resembled the overall shapes of these same distributions in the rat[13].

Grid spacing[17] was defined as the median distance from the center of the autocorrelogram to the six nearest surrounding peaks. The notion of the spacing of a hexagonal grid relies heavily on the assumption that the distances from the center to the nearest neighbors are all roughly equal; to examine this assumption, we computed the ratio between the maximal and minimal distances from the center to any of the nearest six surrounding neighbors, and those neurons which had a ratio larger than 1.5 – that is, they had very elongated hexagonal shapes – were excluded specifically from subsequent analyses of grid-spacing (total of 2/25, or 8% of grid cells); however, these cells *were* included in all other analyses that did not involve spacing. The orientation[17] of the grid was defined as the angle between a fixed reference frame (0^{o} in the autocorrelogram) and the vector to the nearest peak in the counterclockwise direction. The 3 angles of the hexagon were measured between the center of the autocorrelogram and pairs of adjacent peaks in the counter-clockwise direction (Fig 3a). The phase[17] difference represents the relative spatial shift between the rate maps of co-localized grid-cell pairs, and was estimated by analyzing the cross-correlogram of each cell-pair:

$$r(\tau_x,\tau_y)=\frac{n\sum\lambda_1(x,y)\lambda_2(x-\tau_x,y-\tau_y)-\sum\lambda_1(x,y)\sum\lambda_2(x-\tau_x,y-\tau_y)}{\sqrt{n\sum\lambda_1(x,y)^2-(\sum\lambda_1(x,y))^2}\sqrt{n\sum\lambda_2(x-\tau_x,y-\tau_y)^2-(\sum\lambda_2(x-\tau_x,y-\tau_y))^2}}$$

Where $\lambda_1(x,y)$ and $\lambda_2(x,y)$ denote the average rates of neurons 1 and 2 at location (x,y), and τ_x and τ_y denote the spatial lags between the two firing-rate maps. The summation is done over all *n* bins in $\lambda_1(x,y)$ for which the rate was estimated both for $\lambda_1(x,y)$ and $\lambda_2(x-\tau_x,y-\tau_y)$ (i.e., for which the bat spent > 300-ms inside the bin). No smoothing was applied to the cross-correlogram. The phase differences[17] were represented in units of percentages of the maximal possible difference (Fig. 3d): The maximal possible phase difference for each cell-pair was computed by taking the mean of their spacing values and dividing it by a factor of 2 to account for the ambiguity in the direction of phase shift around the center of the cross-correlogram. Because the analysis of phase-difference between two cells is meaningful only if the spacing and orientations of the two neurons are similar, we included in the phase-difference analysis only cell-pairs whose spacing values differed by less than 30% and orientation differed by less than 50% (9/16 pairs, or 56%). Other thresholds were tested and yielded similar results (data not shown).

The effect of the bat's velocity on the firing-rate of grid-cells was assessed by computing the median velocity for each behavioral session in which a grid cell was recorded, and splitting the video and spike data into two equally-sized sets of time epochs (in 2-s windows): A 'high-velocity' set (above the median velocity) and a low-velocity set (below the median velocity). For each of these two sets, we computed the mean firing-rate, and then computed a contrast index of the firing-rates between the high- and low-velocity, defined as:

$$(\mathrm{FiringRate}_{\mathrm{high}} - \mathrm{FiringRate}_{\mathrm{low}}) / (\mathrm{FiringRate}_{\mathrm{High}} + \mathrm{FiringRate}_{\mathrm{Low}})$$

Analysis of head-direction tuning

The bat's head direction was calculated for each video frame by computing the direction of the line perpendicular to the vector connecting the centers of the two light-emitting diodes on the bat's head (the color difference between the two diodes, blue and red, allowed telling apart forward from backward head-direction). The head-direction tuning of a neuron was computed as follows: We binned the data in 3^o bins, and computed the firing-rate in each bin by dividing the number of spikes in that bin by the time the animal spent in that bin. The resulting circular distribution was smoothed using a 10-point hamming window. The peak firing rate was defined as the highest rate in the smoothed head-direction tuning curve. The directionality of this tuning was quantified by computing the mean vector length of the circular distribution[20]:

$$\mathrm{R} = \frac{1}{N} \| \sum_i r_i \|$$

Where r_i is the firing-rate of each bin in the circular distribution of firing rates, and N is the total number of bins in the distribution. The significance of the mean vector length was determined using the same shuffling procedure as the one described above for the gridness index[13,14,19]: Cells were defined as directionally modulated if their vector length index was larger than the 95th percentile of the shuffled distribution (see Supplementary Fig. 12). It should be noted that the degree of directional tuning is likely to be underestimated in our data set, due to the high sensitivity of the mean-vector-length index to background noise spikes: The mean vector length index is much more sensitive to noise spikes than the gridness index (see Supplementary Fig. 20) – and because the firing-rates observed in bat MEC neurons (Figs 2f, 3e, 3g) were generally lower than in rat MEC, probably because of the lower velocities of bat crawling versus rat running, this may explain why the mean vector length in bats (Fig. 3g, *y*-axis of the scatterplot) had lower values than in rats, while the gridness values (Fig. 3g, *x*-axis) were similar in bats and rats[13,14,18,19]. This could also explain the near absence of conjunctive grid × head-direction cells in our dataset.

Analysis of local field potentials

High-frequency ripples were detected in the LFP recordings during sleep, by band-pass filtering the LFP data between 80–160 Hz (Supplementary Fig. 3a and 3d), computing the power of the filtered trace (absolute value of the Hilbert transform), and then defining as ripples those transients that exceeded a threshold of 7 s.d. above the mean power[4,21]. Ripples that were separated by less than 25-ms were merged into one ripple. The duration of each ripple was defined as the duration that the signal power stayed above threshold.

Theta oscillation epochs were identified as follows[4,22]: The LFP was down-sampled by a factor of 2 to a sampling rate of 950 Hz; then the power spectrum was computed in time-windows of 2-s, using Welch's method and a Hamming window with 2,048 samples and 50% overlap. The power in the theta frequency range (4–8 Hz) and in the delta frequency range (2–4 Hz) was computed. Theta epochs were defined as those 2-s windows in which the ratio between the theta power and delta power ("theta-to-delta ratio") exceeded 2.0. Theta tended to occur in short intermittent bouts (Figs 1d, 4c-d); theta-bout durations were computed in increments of 1-s (Fig. 4d), because the theta/delta ratio was calculated in 2-s intervals with 1-sec overlap. Behavioral parameters (bat's velocity and echolocation rate) were computed in the same 2-s windows as the power spectra and the theta-to-delta ratios. For testing the relation between the bat's velocity and theta oscillations, we partitioned the LFP data according to the bat's velocity in each 2-s window, and the corresponding average power spectrum was computed for each velocity range (Figs 1f, 4a-b). We also analyzed the relation between the bat's echolocation call-rate and the LFP (see details in Supplementary Fig. 14). We excluded from LFP analyses any motion artifacts, which were defined as 2-s windows in which the (un-filtered) LFP power exceeded > 10 s.d. above the mean power. Data from the two sleep sessions (pre- and post-behavior) were pooled together both for the analysis of ripples and for the analysis of theta occurrence during sleep. In 2 of the 3 bats in which we recorded from MEC, we conducted simultaneous double-ended LFP recordings (using one of the tetrodes as reference: a tetrode positioned outside the MEC served as reference) and single-ended[23] LFP recordings (where the ground screw served as reference): This is important in order to rule out the possibility that the lack of detectable theta oscillation is due to differential subtraction of two in-phase theta oscillations on the signal-tetrode and reference-tetrode, which is theoretically possible in double-ended recordings, but is impossible in single-ended recordings. Analyses were conducted in the same manner for both the single-ended and double-ended recordings (Fig. 4b, and Supplementary Figs 13 and 14c).

Spectrograms (time × frequency representations) of the theta bouts in Fig. 1d and Fig. 4c were computed using 2,048-point FFT with 97% overlap.

MEC gamma band oscillations[24,25] (25–140 Hz) were readily observed in the LFP recordings from the bat MEC (Supplementary Fig. 21), but were not analyzed further in this paper.

Analysis of spike-train theta modulation

To assess the degree of theta modulation in the spiking patterns of grid-cells recorded in bat MEC, we analyzed the spike-train temporal autocorrelograms. Because most neurons in the rat MEC are theta-modulated[13,26], we also analyzed the multi-unit spike-train temporal autocorrelograms – which are expected to provide a more robust quantification of population-level oscillations in spiking activity, compared to single-unit data, because of the higher firing-rates of multi-units. Bin size of all the temporal autocorrelograms was 10 ms (other bin sizes were tested and yielded similar results). The autocorrelogram was computed for ± 500-ms lags, and the peak of the autocorrelogram at zero lag was equalized to the maximal value not including the zero-lag peak[13,14] (Fig. 4f and Supplementary Fig. 15). The power spectrum of the temporal autocorrelograms was assessed by computing the fast Fourier transform (FFT) of the autocorrelogram, and calculating the square of the FFT magnitude; the length of the FFT was zero padded to 2^{16}. The power spectrum was smoothed with a 2-Hz rectangular window, and the peak value in the 5-11 Hz band was identified. Two methods were used to assess whether a neuron was theta modulated. Method 1: A neuron was defined as theta-modulated if the mean power within 1-Hz of each side of the peak in the 5–11 Hz frequency range was at least 5 times greater than the mean spectral power between 0 Hz and 50 Hz (Fig. 4h, red line) – similar to the 'theta index' used in rat MEC recordings to identify theta modulation of grid-cells[13,14,19,27]. Method 2: A 95% confidence interval was generated for each cell's individual spike train, by randomly jittering the spike timestamps of the original spike train in a range of 20 seconds (±10 seconds on each side), and then re-computing the theta index for each jittered repetition; this process was repeated 500 times per neuron.

Only neurons which showed a theta index higher than the 95% confidence interval, i.e. higher than would be expected by chance, were defined as theta-modulated (see Fig 4h and Supplementary Figs 16–17). Simulations showed that the theta-index measure is quite resilient to noise spikes resulting from spontaneous activity of the neuron, and therefore this index should robustly detect theta modulations, if they are present, even at low firing rates when the temporal structure of the spike train is more susceptible to noise due to spontaneous spiking (Supplementary Fig. 22).

Analysis of theta phase modulation of MEC neurons

To analyze whether MEC neurons were phase-locked to the LFP during theta-bouts, we extracted individual theta-bout windows (2-s windows where the theta-to-delta ratio > 2, see above). We filtered the LFP between 4-10 Hz (while eliminating edge effects of the filtering by taking broad margins), and then each spike was assigned a phase relative to the filtered signal, with 0° and 180° referring to the peak and troughs of the signal, respectively (Fig. 4i and Supplementary Fig. 18). Bin size = 60°. Data from theta-bouts in all three sessions (2 sleep sessions and the behavioral session) were pooled together. For the phase analysis in Fig. 4i and Supplementary Fig. 18, we combined for each neuron the data from all three sessions, because for most cells it was impossible to construct reliable histograms based on the very few spikes that were emitted during theta-bouts in the behavioral session alone (because the theta bouts were very sparse: Fig. 4c-e). Only neurons that fired 5 or more spikes per phase-bin on average, were included in the analysis (n=12 cells). Same analysis was done for the non-theta-bout epochs (theta to delta ratio < 2) where again only neurons that fired 5 or more spikes per phase bin on average were included in the analysis (n=54 cells). The non-theta-bout analysis was conducted to verify that the lack of strong theta modulation was not due to an overly strict theta-detection threshold (see above), as well as to provide evidence for the accurate detection of the theta-bouts, which was indeed supported by the finding that theta modulation was detected only during the identified theta-bouts (Fig. 4i).

Analysis of the effect of theta-bouts removal

To test the significance of the removal of theta-bout epochs on the grid structure, we compared the gridness before and after the removal of all theta-bouts. For each grid cell we removed all spikes and positional data that occurred during the theta-bout epochs, and the new “theta-free” data were used to re-compute the firing-rate maps and their spatial autocorrelograms and gridness indexes (Fig. 4j-k and Supplementary Fig. 19). To test for the statistical significance of the removal of theta-bouts, the change in gridness for each neuron was compared to a 95% confidence interval generated for each neuron separately using a bootstrap procedure where we randomly removed time-epochs of equal durations to those of the theta-bouts (1,000 repetitions of the random removal for each grid-cell), as shown in Fig. 4l. A change in gridness was considered significant if the actual new gridness (Fig. 4l, blue dots) was outside the 95% confidence interval (Fig. 4l, orange area); in none of the grid-cells did we observe a significant change in gridness after theta-bout removal.

Histology for reconstruction of tetrode tracks

Electrodes were not moved after the final recording session. The bats were given an overdose of sodium pentobarbital and, with tetrodes left *in situ*, were perfused transcardially using a flush of 50 ml phosphate buffer saline followed by 200 ml of fixative (4% paraformaldehyde + 0.1 M phosphate buffer saline). The brains were removed and stored in fixative. Subsequently, a coronal block (for hippocampal CA1 recordings) or the entire right hemisphere (for MEC recordings) was embedded in paraffin, and then 10 µM sections were cut (coronal sections for CA1 bats and sagittal sections for MEC bats); every 3rd section was then mounted on glass slides, resulting in 30 µM intervals between adjacent mounted slides. The sections were then Nissl-stained with cresyl violet, and coverslipped.

A light microscope fitted with a digital camera was used to determine tetrode placement in the CA1 pyramidal layer (2 bats; see example in Fig. 1a) or in the MEC (3 bats; see examples in Fig. 2b-d and Supplementary Figs 7–8). Most of the MEC data were recorded at the last 80–100% portions of the visible tetrode track. The exact positioning of tetrodes on each recording day was extrapolated using the documentation of daily tetrode-turning for each animal, while taking into account shrinkage of the tissue as a result of histological procedures (10–20% shrinkage). For MEC track reconstruction, in 50% of the recording tetrodes (2/4) the exact positioning of the tetrodes was also verified using an electrolytic lesion (DC current, 30 µA, 15-s duration) made at the last recording position (Fig. 2b, and Supplementary Fig. 7 section #8 - green circle). The distance between the position of each recorded neuron and the postrhinal border of

MEC (dorsal border), was measured in the same section parallel to the pial surface along the layer where the tetrode was located.

Anatomical delineation of the medial entorhinal cortex

A separate group of 8 naïve adult bats were perfused as explained above, and immuno-staining was performed on equally spaced series of 50-μm thick sagittal sections, cut on a freezing sliding microtome. Sections were incubated with monoclonal mouse primary antibodies against parvalbumin (Sigma-Aldrich P3088, 1:2000 in TBS-TX) or with polyclonal rabbit primary antibodies against calretinin (Millipore C2724, 1:1000), followed by respectively a secondary goat anti-mouse antibody coupled to biotin (Sigma Aldrich B7151, 1:100), or a secondary goat anti-rabbit antibody coupled to biotin (Sigma Aldrich B 8895, 1:800); they were visualized with the Vector ABC kit (Vector laboratories, Peroxidase standard PK-Vectastain ABC kit 400), reacted with diaminobenzidine, and mounted on glass slides with a 0.2% gelatin solution. The sections were subsequently air-dried, dehydrated through increasing concentrations of ethanol, and embedded in Entellan[28,29].

The laminar location of the recording tetrodes in MEC was determined on the basis of cytoarchitectonic criteria (Supplementary Fig. 6 and ref. 29). Layer II of MEC is characterized by fairly large, densely packed neurons that stain densely for Nissl substance. Layer III is a wider layer consisting of regularly arranged, lightly stained large-to-medium sized cells predominantly pyramidal shaped. At the deep border of layer III is the cell-sparse fiber layer called the *lamina dissecans*. Layer V is multi-laminated and comprises different sizes of pyramidal cells that show a radial arrangement. Layer VI comprises a wider variety of neuron-types of different sizes that are oriented parallel to the pial surface. The border between MEC and the dorsally adjacent postrhinal cortex was determined by the abrupt cessation of the *lamina dissecans*, coinciding with a marked reduction in parvalbumin staining and increased staining intensity for calretinin (Fig. 2a, and Supplementary Figs 5 and 6).

Supplementary Text

High-frequency ripples in CA1 and MEC of Egyptian fruit bats are very similar to ripples in CA1 and MEC of rats:

In CA1 of Egyptian fruit bats, high-frequency ripple oscillations (120–160 Hz) were present in the local field potential (LFP) during sleep (Supplementary Fig. 3a), and were very similar in their properties to ripples in the rat hippocampus: the ripples often occurred in doublets, they were associated with hippocampal sharp-waves, and were accompanied by an increase in neuronal firing-rate that was phase-locked to the ripples' oscillatory cycles (Supplementary Fig. 3b,c) – similar to ripples in rat hippocampus[21]. Ripples in bat MEC were readily present in the LFP during sleep (Supplementary Fig. 3d) and had a frequency range of 120–160 Hz , similar to the frequency range of ripples in bat CA1[4] and similar to ripples in rat MEC[32]. MEC ripples often occurred in doublets, and co-occurred with increased firing-rate of MEC neurons (Supplementary Fig. 3e,f). Ripple durations were 37.4 ± 20.9 ms, similar to rat MEC[32]. Further, as in rats[32], ripples in bat MEC had shorter duration than ripples in bat CA1 (44.4 ± 18.6 ms; t-test, $t(2386) = 6.8$, $P < 10^{-11}$; Supplementary Fig. 3g) and were more variable.

References

1. Ulanovsky, N. & Moss, C.F. What the bat's voice tells the bat's brain. *Proc. Natl. Acad. Sci. USA* **105,** 8491-8498 (2008).
2. Altringham, J.D. *Bats: Biology and Behaviour* (Oxford University Press, Oxford, 1996).
3. Neuweiler, G. *The Biology of Bats* (Oxford University Press, Oxford, 2000).
4. Ulanovsky, N. & Moss, C.F. Hippocampal cellular and network activity in freely moving echolocating bats. *Nature Neurosci.* **10**, 224-233 (2007).
5. Ulanovsky, N. & Moss, C.F. Dynamics of hippocampal spatial representation in echolocating bats. *Hippocampus* **21,** 150-161 (2011).
6. Baron, G., Stephan, H. & Frahm, H.D. *Comparative Neurobiology in Chiroptera, Vol. 3* (Birkhauser Verlag, Basel, 1996).
7. Muller, R.U., Kubie, J.L. & Ranck, J.B., Jr. Spatial firing patterns of hippocampal complex-spike cells in a fixed environment. *J. Neurosci.* **7,** 1935-1950 (1987).
8. Fyhn, M., Molden, S., Witter, M.P., Moser, E.I. & Moser, M.-B. Spatial representation in the entorhinal cortex. *Science* **305,** 1258-1264 (2004).
9. Holland, R.A., Winter, P. & Waters, D.A. Sensory systems and spatial memory in the fruit bat *Rousettus aegyptiacus*. *Ethology* **111,** 715-725 (2005).
10. Holland, R.A., Waters, D.A. & Rayner, J.M. Echolocation signal structure in the Megachiropteran bat *Rousettus aegyptiacus* Geoffroy 1810. *J. Exp. Biol.* **207,** 4361-4369 (2004).
11. Yovel, Y., Falk, B., Moss, C.F. & Ulanovsky, N. Optimal localization by pointing off axis. *Science* **327,** 701-704 (2010).
12. Schnitzer-Torbert, N., Jackson, J., Henze, D., Harris, K.D. & Redish, A.D. Quantitative measures of cluster quality for use in extracellular recordings. *Neuroscience* **131,** 1-11 (2005).
13. Boccara, C.N. *et al.* Grid cells in pre- and parasubiculum. *Nature Neurosci.* **13,** 987-994 (2010).
14. Langston, R.F. *et al.* Development of the spatial representation system in the rat. *Science* **328,** 1576-1580 (2010).
15. Skaggs, W.E., McNaughton, B.L., Wilson, M.A. & Markus, E.J. An information-theoretic approach to deciphering the hippocampal code. In: *Advances in neural information processing systems 5*, edited by S.J. Hanson, J.D. Cowan & C. L. Giles (Morgan Kaufman, San Mateo, 1993), pp. 1030-1037.
16. Skaggs, W.E., McNaughton, B.L., Wilson, M.A. & Barnes, C.A. Theta phase precession in hippocampal neuronal populations and the compression of temporal sequences. *Hippocampus* **6,** 149-172 (1996).
17. Hafting, T., Fyhn, M., Molden, S., Moser, M.-B., & Moser, E.I. Microstructure of a spatial map in the entorhinal cortex. *Nature* **436,** 801-806 (2005).

18. Sargolini, F. *et al.* Conjunctive representation of position, direction, and velocity in entorhinal cortex. *Science* **312,** 758-762 (2006).

19. Wills, T.J., Cacucci, F., Burgess, N. & O'Keefe, J. Development of the hippocampal cognitive map in preweanling rats. *Science* **328,** 1573-1576 (2010).

20. Fisher, N.I. *Statistical Analysis of Circular Data* (Cambridge University Press, 1995).

21. Csicsvari, J., Hirase, H., Czurkó, A., Mamiya, A. & Buzsáki, G. Fast network oscillations in the hippocampal CA1 region of the behaving rat. *J. Neurosci.* **19,** RC20 (1999).

22. Csicsvari, J., Hirase, H., Czurkó, A., Mamiya, A. & Buzsáki, G. Oscillatory coupling of hippocampal pyramidal cells and interneurons in the behaving Rat. *J. Neurosci.* **19,** 274-287 (1999).

23. Hafting, T., Fyhn, M., Bonnevie, T., Moser, M.-B., & Moser, E.I., Hippocampus-independent phase precession in entorhinal grid cells. *Nature* **453,** 1248-1252 (2008).

24. Colgin, L.L. *et al*. Frequency of gamma oscillations routs flow of information in the hippocampus. *Nature* **462,** 353-357 (2009).

25. Chrobak, J.J. & Buzsáki, G. Gamma oscillations in the entorhinal cortex of the freely behaving rat. *J. Neurosci.* **18**, 388-398 (1998).

26. Frank, L.M., Brown, E.N. & Wilson, M.A. A comparison of the firing properties of putative excitatory and inhibitory neurons from CA1 and the entorhinal cortex. *J. Neurophysiol.* **86,** 2029-2040 (2001).

27. Deshmukh, S.S., Yoganarasimha, D., Voicu, H. & Knierim, J.J. Theta modulation in the medial and the lateral entorhinal cortices. *J. Neurophysiol.* **104,** 994-1006 (2010).

28. Wouterlood, F.G., Hartig, W., Bruckner, G. & Witter, M.P. Parvalbumin-immunoreactive neurons in the entorhinal cortex of the rat: localization, morphology, connectivity and ultrastructure. *J. Neurocytol.* **24,** 135-153 (1995).

29. Kjonigsten, J.L., Leergaard, B.T., Witter, M.P. & Bjaalie, G.J. Digital atlas of anatomical subdivisions and boundaries of the rat hippocampal region. *Front. Neuroinformatics* **5**:2, 1 (2011).

30. Gatome, C.W., Slomianka, L., Mwangi, D.K., Lipp, H.-P., & Amrein, I. The entorhinal cortex of the Megachiroptera: a comparative study of Wahlberg's epauletted fruit bat and the straw-coloured fruit bat. *Brain Struct. Funct.* **214,** 375-393 (2010).

31. Buzsáki, G. *et al.* Hippocampal network patterns of activity in the mouse. *Neuroscience* **116,** 201-211 (2003).

32. Chrobak, J.J. & Buzsáki, G. High-frequency oscillations in the output networks of the hippocampal-entorhinal axis of the freely behaving rat. *J. Neurosci.* **16,** 3056-3066 (1996).

33. Witter, M.P., Wouterlood, F.G., Naber, P.A. & Van Haeften, T. Anatomical organization of the parahippocampal-hippocampal network. *Ann. NY Acad. Sci.* **911,** 1-24 (2000).

34. Burwell, R.D. Borders and cytoarchitecture of the perirhinal and postrhinal cortices in the rat. *J. Comp. Neurol*. **437,** 17-41 (2001).

35. Brandon, M.P. *et al*. Reduction of theta rhythm dissociates grid cell spatial periodicity from directional tuning. *Science* **332,** 595-599 (2011).

36. Mizuseki, K., Sirota, A., Pastalkova, E. & Buzsáki, G. Theta oscillations provide temporal windows for local circuit computation in the entorhinal-hippocampal loop. *Neuron* **64,** 267-280 (2009).

37. Derdikman, D. *et al.* Fragmentation of grid cell maps in a multicompartment environment. *Nature Neurosci.* **12**, 1325-1332 (2009).

38. Jeewajee, A., Barry, C., O'Keefe, J. & Burgess, N. Grid cells and theta as oscillatory interference: electrophysiological data from freely moving rats. *Hippocampus* **18**, 1175-1185 (2008)

39. Doeller, C.F., Barry, C. & Burgess, N. Evidence for grid cells in a human memory network. *Nature* **463**, 657-661 (2010).